bioRxiv preprint doi: https://doi.org/10.1101/051631; this version posted May 4, 2016. The copyright holder for this preprint (which was not certified by peer review) is the author/funder, who has granted bioRxiv a license to display the preprint in perpetuity. It is made available under aCC-BY-NC-ND 4.0 International license.

Clustering RNA-seq expression data using grade of membership models

Kushal K Dey[1] Chiaowen Joyce Hsiao[2] Matthew Stephens[1,2]

[1] Department of Statistics, University of Chicago, Chicago, Illinois 60637, USA; [2] Department of Human Genetics, University of Chicago, Chicago, Illinois 60637, USA

Keywords: Admixture model, Clustering, Gene expression, Grade of membership model, Latent Dirichlet Allocation, Topic models, RNA-seq, Single cell

Corresponding Author: Email mstephens@uchicago.edu

bioRxiv preprint doi: https://doi.org/10.1101/051631; this version posted May 4, 2016. The copyright holder for this preprint (which was not certified by peer review) is the author/funder, who has granted bioRxiv a license to display the preprint in perpetuity. It is made available under aCC-BY-NC-ND 4.0 International license.

Abstract

Grade of membership models, also known as "admixture models", "topic models" or "Latent Dirichlet Allocation", are a generalization of cluster models that allow each sample to have membership in multiple clusters. These models are widely used in population genetics to model admixed individuals who have ancestry from multiple "populations", and in natural language processing to model documents having words from multiple "topics". Here we illustrate the potential for these models to cluster samples of RNA-seq gene expression data, measured on either bulk samples or single cells. We also provide methods to help interpret the clusters, by identifying genes that are distinctively expressed in each cluster. By applying these methods to several example RNA-seq applications we demonstrate their utility in identifying and summarizing structure and heterogeneity. Applied to data from the GTEx project on 51 human tissues, the approach highlights similarities among biologically-related tissues and identifies distinctively-expressed genes that recapitulate known biology. Applied to single-cell expression data from mouse preimplantation embryos, the approach highlights both discrete and continuous variation through early embryonic development stages, and highlights genes involved in a variety of relevant processes – from germ cell development, through compaction and morula formation, to the formation of inner cell mass and trophoblast at the blastocyte stage. The methods are implemented in the Bioconductor package `CountClust`.

1 Introduction

Ever since large-scale gene expression measurements have been possible, clustering – of both genes and samples – has played a major role in their analysis [3–5]. For example, clustering of genes can identify genes that are working together or are co-regulated, and clustering of samples is useful for quality control as well as identifying biologically-distinct subgroups. A wide range of clustering methods have therefore been employed in this context, including distance-based hierarchical clustering, k-means clustering, and self-organizing maps (SOMs); see for example [6, 7] for reviews.

Here we focus on cluster analysis of samples, rather than clustering of genes (although our methods do highlight sets of genes that distinguish each cluster). Traditional clustering methods for this problem attempt to partition samples into distinct groups that show "similar" expression patterns. While partitioning samples in this way has intuitive appeal, it seems likely that the structure of a typical gene expression data set will be too complex to be fully captured by such a partitioning. Motivated by this, here we analyse expression data using grade of membership (GoM) models [8], which generalize clustering models to allow each sample to have partial membership in multiple clusters. That is, they allow that each sample has a proportion, or "grade" of membership in each cluster. Such models are widely used in population genetics to model admixture, where individuals can have ancestry from multiple populations [14], and in document clustering [32, 33] where each document can have membership in multiple topics. In these fields GoM models are often known as "admixture models", and "topic models" or "Latent Dirichlet Allocation" [32]. GoM models have also recently been applied to detect mutation signatures in cancer samples [31].

Although we are not the first to apply GoM-like models to gene expression data, previous applications have been primarily motivated by a specific goal, "cell type deconvolution", which involves using cell-type-specific expression profiles of marker genes to estimate the proportions of different cell types in a mixture [38, 40, 41]. Specifically, the GoM model we use here is analogous to – although different in detail from – blind deconvolution approaches [36, 37, 39] which estimate cell type proportions and cell type signatures jointly (see also [34, 35] for semi-supervised approaches). Our goal here is to

bioRxiv preprint doi: https://doi.org/10.1101/051631; this version posted May 4, 2016. The copyright holder for this preprint (which was not certified by peer review) is the author/funder, who has granted bioRxiv a license to display the preprint in perpetuity. It is made available under aCC-BY-NC-ND 4.0 International license.

demonstrate that GoM models can be useful much more broadly for understanding structure in RNA-seq data – not only to deconvolve mixtures of cell types. For example, in our analysis of human tissue samples from the GTEX project below, the GoM model usefully captures biological heterogeneity among samples even though the inferred grades of membership are unlikely to correspond precisely to proportions of specific cell types. And in our analyses of single-cell expression data the GoM model highlights interesting structure, even though interpreting the grades of membership as "proportions of cell types" is clearly inappropriate because each sample is a single cell! Here we are exploiting the GoM as a flexible extension of traditional cluster models, which can capture "continuous" variation among cells as well as the more "discrete" variation captured by cluster models. Indeed, the extent to which variation among cells can be described in terms of discrete clusters versus more continuous populations is a fundamental question that, when combined with appropriate single-cell RNA-seq data, the GoM models used here may ultimately help address.

2 Methods Overview

We assume that the RNA-seq data on N samples has been summarized by a table of counts $C_{N\times G} = (c_{ng})$, where c_{ng} is the number of reads from sample n mapped to gene g (or other unit, such as transcript or exon) [12]. The GoM model is a generalization of a cluster model, which allows that each sample has some proportion ("grade") of membership, in each cluster. For RNA-seq data this corresponds to assuming that each sample n has some proportion of its reads, q_{nk} coming from cluster k. In addition, each cluster k is characterized by a probability vector, $\theta_{k\cdot}$, whose gth element represents the relative expression of gene g in cluster k. The GoM model is then

$$(c_{n1}, c_{n2}, \cdots, c_{nG}) \sim \text{Multinomial}\,(c_{n+}, p_{n1}, p_{n2}, \cdots, p_{nG})\,, \tag{1}$$

where $c_{n+} = \sum_{g=1}^{G} c_{ng}$ and we assume

$$p_{ng} := \sum_{k=1}^{K} q_{nk}\theta_{kg}. \tag{2}$$

The number of clusters K is set by the analyst, and it can be helpful to explore multiple values of K (see Discussion).

To fit this model to RNA-seq data, we exploit the fact that exactly the same GoM model is commonly used for document clustering [32]. This is because, just as RNA-seq samples can be summarized by counts of reads mapping to each possible gene in the genome, document data can be summarized by counts of each possible word in a dictionary. Recognizing this allows existing methods and software for document clustering to be applied directly to RNA-seq data. Here we use the R package `maptpx` [13] to fit the GoM model.

Fitting the GoM model results in estimated membership proportions q for each sample, and estimated expression values θ for each cluster. We visualize the membership proportions for each sample using a "Structure plot" [15], which is named for its widespread use in visualizing the results of the *Structure* software [14] in population genetics. The Structure plot represents the estimated membership proportions of each sample as a stacked barchart, with bars of different colors representing different clusters. Consequently, samples that have similar membership proportions have similar amounts of each color. See Fig 1 for example.

To help biologically interpret the clusters inferred by the GoM model we also implemented methods to identify, for each cluster, which genes are most distinctively differentially expressed in that cluster

bioRxiv preprint doi: https://doi.org/10.1101/051631; this version posted May 4, 2016. The copyright holder for this preprint (which was not certified by peer review) is the author/funder, who has granted bioRxiv a license to display the preprint in perpetuity. It is made available under aCC-BY-NC-ND 4.0 International license.

(see Methods). Functions for fitting the GoM model, plotting the structure plots, and identifying the distinctive ("driving") genes in each cluster, are included in our R package `CountClust` [44] available through Bioconductor [29].

3 Results

3.1 Clustering human tissue samples using bulk RNA-seq

We begin by illustrating the GoM model on bulk RNA expression measurements from the GTEx project (V6 dbGaP accession phs000424.v6.p1, release date: Oct 19, 2015, `http://www.gtexportal.org/home/`). These data consist of per-gene read counts from RNA-seq performed on $8,555$ samples collected from 450 human donors across 51 tissues, lymphoblastoid cell lines, and transformed fibroblast cell-lines. We analyzed $16,069$ genes that satisfied filters (e.g. exceeding certain minimum expression levels) that were used during eQTL analyses by the GTEx project (gene list available in `http://stephenslab.github.io/count-clustering/project/utilities/gene_names_all_gtex.txt`).

We fit the GoM model to these data, with number of clusters $K = 5, 10, 15, 20$. For each K we ran the fitting algorithm three times and kept the result with the highest log-likelihood. Fig 1(a) shows the Structure plot for $K = 20$, with results for other K in S1 Fig. (See also `http://stephenslab.github.io/count-clustering/project/src/tissues_tSNE_2.html` for an alternative visualization using a 2-dimensional projection with t-SNE [20, 21].)

In all cases results reflect the known division of samples into tissues: that is, samples from the same tissue tend to have similar cluster membership proportions. As might be expected, increasing K highlights finer structure in the data, with tissues that cluster together with smaller K being subdivided into distinct subgroups for larger K. For brevity we focus on results for $K = 20$ (Fig 1(a)). Here some tissues are represented by essentially a single cluster (e.g. Pancreas, Liver), whereas other tissues are represented as a mixture of multiple clusters (e.g. Thyroid, Spleen). Furthermore, the results highlight biological similarity among some tissues by assigning similar membership proportions to samples from those tissues. For example, samples from several different parts of the brain often have similar memberships, as do the arteries (aorta, tibial and coronary) and skin samples (sun-exposed and un-exposed).

To help biologically interpret results we implemented methods to identify the genes and genetic processes that characterize each cluster (see Methods). Table 1 summarizes results for the GTEx results in Fig 1a (see also S1 Table). Reassuringly, many results align with known biology. For example, the purple cluster (cluster 18), which distinguishes Pancreas from other tissues, is enriched for genes responsible for digestion and proteolysis, (e.g. *PRSS1*, *CPA1*, *PNLIP*). Similarly the yellow cluster (cluster 12), which primarily distinguishes Cell EBV Lymphocytes from other tissues, is enriched with genes responsible for immune responses (e.g. *IGHM*, *IGHG1*) and the pink cluster (cluster 19) which mainly shows up in Whole Blood, is enriched with genes related hemoglobin complex and oxygen transport (e.g. *HBB*, *HBA1*, *HBA2*). Further, Keratin-related genes characterize the skin cluster (cluster 6, light denim), Myosin-related genes characterize the muscle skeletal cluster (cluster 7, orange), etc. The royal purple cluster (cluster 1) has memberships in most tissues and the genes distinguishing the cluster seem to be responsible for nucleus and nucleoplasm related functionality. In cases where a cluster occurs in multiple tissues these biological annotations may be particularly helpful

bioRxiv preprint doi: https://doi.org/10.1101/051631; this version posted May 4, 2016. The copyright holder for this preprint (which was not certified by peer review) is the author/funder, who has granted bioRxiv a license to display the preprint in perpetuity. It is made available under aCC-BY-NC-ND 4.0 International license.

for understanding what is driving this co-membership. For example, the top genes in the red cluster (cluster 3), which is common to Breast Mammary tissue, Adipose Subcutaneous and Adipose Visceral, are related to adipocytes and/or fatty acid synthesis; and the top genes in the salmon cluster (cluster 4), which is common to the Gastroesophageal Junction, Esophagus Muscularis and Colon Sigmoid, are related to smooth muscle.

Although global analysis of all tissues is useful for highlighting major structure in the data, it may miss finer-scale structure within tissues or among similar tissues. For example, here the global analysis allocated only three clusters to all brain tissues (clusters 1,2 and 9 in Fig 1(a)), and we suspected that additional substructure might be uncovered by analyzing the brain samples separately with larger K. Fig 1(b) shows the Structure plot for $K = 6$ on only the Brain samples. The results highlight much finer-scale structure compared with the global analysis. Brain Cerebellum and Cerebellar hemisphere are essentially assigned to a separate cluster (lime green), which is enriched with genes related to cell periphery and communication (e.g. *PKD1*, *CBLN3*) as well as genes expressed largely in neuronal cells and playing a role in neuron differentiation (e.g. *CHGB*). The spinal cord samples also show consistently strong membership in a single cluster (yellow-orange), the top defining gene for the cluster being *MBP* which is involved in myelination of nerves in the nervous system [42]. Another driving gene, *GFAP*, participates in system development by acting as a marker to distinguish astrocytes during development [2].

The remaining samples all show membership in multiple clusters. Samples from the putamen, caudate and nucleus accumbens show similar profiles, and are distinguished by strong membership in a cluster (cluster 4, bright red) whose top driving gene is *PPP1R1B*, a target for dopamine. And cortex samples are distinguished from others by stronger membership in a cluster (cluster 2, turquoise in Fig 1(b)) whose distinctive genes include *ENC1*, which interacts with actin and contributes to the organisation of the cytoskeleton during the specification of neural fate [1].

3.2 Quantitative comparison with hierarchical clustering

We used the GTEx data to test whether the GoM model is more accurate in detecting substructure than distance-based clustering methods. Specifically, for each pair of tissues in the GTEx data we assessed whether or not each clustering method correctly partitioned samples into the two tissue groups (see Methods). The GoM model was substantially more accurate in this test, succeeding in 81% of comparisons, compared with 29% for the distance-based method (Fig 2). This presumably reflects the general tendency for model-based approaches to be more efficient that distance-based approaches, provided that the model is sufficiently accurate.

3.3 Clustering of single-cell RNA-seq data

Recently RNA-sequencing has become viable for single cells [9], and this technology has the promise to revolutionize understanding of intra-cellular variation in expression, and regulation more generally [10]. Although it is traditional to describe and categorize cells in terms of distinct cell-types, the actual architecture of cell heterogeneity may be more complex, and in some cases perhaps better captured by the more "continuous" GoM model. In this section we illustrate the potential for the GoM model to be applied to single cell data.

To be applicable to single-cell RNA-seq data, methods must be able to deal with lower sequencing

bioRxiv preprint doi: https://doi.org/10.1101/051631; this version posted May 4, 2016. The copyright holder for this preprint (which was not certified by peer review) is the author/funder, who has granted bioRxiv a license to display the preprint in perpetuity. It is made available under aCC-BY-NC-ND 4.0 International license.

depth than in bulk RNA experiments: single-cell RNA-seq data typically involve substantially lower effective sequencing depth compared with bulk experiments, due to the relatively small number of molecules available to sequence in a single cell. Therefore, as a first step towards demonstrating its potential for single cell analysis, we checked robustness of the GoM model to sequencing depth. Specifically, we repeated the analyses above after thinning the GTEx data by a factor of 100 and $10,000$ to mimic the lower sequencing depth of a typical single cell experiment. For the thinned GTEx data the Structure plot for $K = 20$ preserves most of the major features of the original analysis on unthinned data (S2 Fig). For the accuracy comparisons with distance-based methods, both methods suffer reduced accuracy in thinned data, but the GoM model remains superior (S3 Fig). For example, when thinning by a factor of $10,000$, the success rate in separating pairs of tissues is 0.32 for the GoM model vs 0.10 for hierarchical clustering.

Having established its robustness to sequencing depth, we now illustrate the GoM model on two single cell RNA-seq datasets, from Jaitin *et al* [22] and Deng *et al* [23].

3.3.1 Jaitin et al, 2014

Jaitin *et al* sequenced over $4,000$ single cells from mouse spleen. Here we analyze $1,041$ of these cells that were categorized as $CD11c+$ in the *sorting markers* column of their data (`http://compgenomics.weizmann.ac.il/tanay/?page_id=519`), and which had total number of reads mapping to non-ERCC genes greater than 600. We believe these cells correspond roughly to the $1,040$ cells in their Figure S7. Our hope was that applying our method to these data would identify, and perhaps refine, the cluster structure evident in [22] (their Figures 2A and 2B). However, our method yielded rather different results (Fig 3), where most cells were assigned to have membership in several clusters. Further, the cluster membership vectors showed systematic differences among amplification batches (which in these data is also strongly correlated with sequencing batch). For example, cells in batch 1 are characterized by strong membership in the orange cluster (cluster 5) while those in batch 4 are characterized by strong membership in both the blue and yellow clusters (2 and 6). Some adjacent batches show similar patterns - for example batches 28 and 29 have a similar visual "palette", as do batches 32-45. And, more generally, these later batches are collectively more similar to one another than they are to the earlier batches (0-4).

The fact that batch effects are detectable in these data is not particularly surprising: there is a growing recognition of the importance of batch effects in high-throughput data generally [26] and in single cell data specifically [27]. And indeed, both clustering methods and the GoM model can be viewed as dimension reduction methods, and such methods can be helpful in controlling for batch effects [24, 25]. However, why these batch effects are not evident in Figures 2A and 2B of [22] is unclear.

3.3.2 Deng et al, 2014

Deng *et al* collected single-cell expression data of mouse preimplantation embryos from the zygote to blastocyst stage [23], with cells from four different embryos sequenced at each stage. The original analysis [23] focusses on trends of allele-specific expression in early embryo development. Here we use the GoM model to assess the primary structure in these data without regard to allele-specific effects (i.e. combining counts of the two alleles). Visual inspection of the Principal Components Analysis in [23] suggested perhaps 6-7 clusters, and we focus here on results with $K = 6$.

bioRxiv preprint doi: https://doi.org/10.1101/051631; this version posted May 4, 2016. The copyright holder for this preprint (which was not certified by peer review) is the author/funder, who has granted bioRxiv a license to display the preprint in perpetuity. It is made available under aCC-BY-NC-ND 4.0 International license.

The results from the GoM model (Fig 4) clearly highlight changes in expression profiles that occur through early embryonic development stages, and enrichment analysis of the driving genes in each cluster (Table 3, S3 Table) indicate that many of these expression changes reflect important biological processes during embryonic preimplantation development.

In more detail: Initially, at the zygote and early 2-cell stages, the embryos are represented by a single cluster (blue in Fig 4) that is enriched with genes responsible for germ cell development (e.g., *Bcl2l10* [52], *Spin1* [53]). Moving through subsequent stages the grades of membership evolve to a mixture of blue and magenta clusters (mid 2-cell), a mixture of magenta and yellow clusters (late 2-cell) and a mixture of yellow and green (4-cell stage). The green cluster then becomes more prominent in the 8-cell and 16-cell stages, before dropping substantially in the early and mid-blastocyst stages. That is, we see a progression in the importance of different clusters through these stages, from the blue cluster, moving through magenta and yellow to green. By examining the genes distinguishing each cluster we see that this progression reflects the changing relative importance of several fundamental biological processes. The magenta cluster is driven by genes responsible for the beginning of transcription of zygotic genes (e.g., *Zscan4c-f* show up in the list of top 100 driving genes : see `https://stephenslab.github.io/count-clustering/project/src/deng_cluster_annotations.html`), which takes place in the late 2-cell stage of early mouse embryonic development [55]. The yellow cluster is enriched for genes responsible for heterochromation *Smarcc1* [56] and chromosome stability *Cenpe* [57] (see S3 Table) . And the green cluster is enriched for cytoskeletal genes (e.g., *Fbxo15*) and cytoplasm genes (e.g., *Tceb1*, *Hsp90ab1*), all of which are essential for compaction at the 8-cell stage and morula formation at the 16-cell stage.

Finally, during the blastocyst stages two new clusters (purple and orange in Fig 4) dominate. The orange cluster is enriched with genes involved in the formation of outer trophoblast cells (e.g., *Tspan8*, *Krt8*, *Id2* [50]), while the purple cluster is enriched with genes responsible for the formation of inner cell mass (e.g., *Pdgfra*, *Pyy* [51]). Thus these two clusters are consistent with the two cell lineages, the trophectoderm and the primitive endoderm, that make up the majority of the cells of the blastocyst [54]. Interestingly, however, the cells do not appear to fall into two distinct and clearly-separated populations – at least, not in terms of their expression patterns – but rather show a continuous range of memberships in these two clusters, even in the late blastocyst stage.

In addition to these trends across development stages, the GoM results also highlight some embryo-level effects in the early stages (Fig 4). Specifically, cells from the same embryo sometimes show greater similarity than cells from different embryos. For example, while all cells from the 16-cell stage have high memberships in the green cluster, cells from two of the embryos at this stage have memberships in both the purple and yellow clusters, while the other two embryos have memberships only in the yellow cluster.

Finally, we note that, like clustering methods, the GoM model can be helpful in exploratory data analysis and quality control. Indeed, the GoM results highlight a few single cells as outliers. For example, a cell from a 16-cell embryo is represented by the blue cluster - a cluster that represents cells at the zygote and early 2-cell stage. Also, a cell from an 8-stage embryo has strong membership in the purple cluster - a cluster that represents cells from the blastocyst stage. It would seem prudent to consider excluding these cells from subsequent analyses of these data.

bioRxiv preprint doi: https://doi.org/10.1101/051631; this version posted May 4, 2016. The copyright holder for this preprint (which was not certified by peer review) is the author/funder, who has granted bioRxiv a license to display the preprint in perpetuity. It is made available under aCC-BY-NC-ND 4.0 International license.

4 Discussion

Our goal here is to highlight the potential for GoM models to elucidate structure in RNA-seq data from both single cell sequencing and bulk sequencing of pooled cells. We also provide tools to identify which genes are most distinctively expressed in each cluster, to aid interpretation of results. As our applications illustrate, these methods have the potential to highlight biological processes underlying the cluster structure identified.

The GoM model has several advantages over distance-based hierarchical methods of clustering. At the most basic level model-based methods are often more accurate than distance-based methods. Indeed, in our simple test on the GTEx data the model-based GoM approach more accurately separated samples into "known" clusters. However, there are also other subtler benefits of the GoM model. Because the GoM model does not assume a strict "discrete cluster" structure, but rather allows that each sample has a proportion of membership in each cluster, it can provide insights into how well a particular dataset really fits a "discrete cluster" model. For example, consider the results for the data from Jaitin *et al* [22] and Deng *et al* [23]: in both cases most samples are assigned to multiple clusters, although the results are closer to "discrete" for the latter than the former. The GoM model is also better able to represent the situation where there is not really a single clustering of the samples, but where samples may cluster differently at different genes. For example, in the GTEx data, the stomach samples share memberships in common with both the pancreas (purple) and the adrenal gland (light green). This pattern can be seen in the Structure plot (Fig 1) but would be hard to discern from a standard hierarchical clustering.

GoM models also have close connections with dimension reduction techniques such as factor analysis, principal components analysis and non-negative matrix factorization. All of these methods can also be used for RNA-seq data, and may often be useful. See [19] for discussion of relationships among these methods in the context of inferring population genetic structure. While not arguing that the GoM model is uniformly superior to these other methods, we believe our examples illustrate the appeals of the approach. In particular, we would argue that for the GTEx data, the Structure plot (Fig 1) combined with the cluster annotations (Table 1) provide a more visually and biologically appealing summary of the data than would a principal components analysis.

Fitting GoM models can be computationally-intensive for large data sets. For the datasets we considered here the computation time ranged from 12 minutes for the data from [23] ($n = 259; K = 6$), through 33 minutes for the data from [22] ($n = 1,041; K = 7$) to 3,370 minutes for the GTEx data ($n = 8,555; K = 20$). Computation time can be reduced by fitting the model to only the most highly expressed genes, and we often use this strategy to get quick initial results for a dataset. Because these methods are widely used for clustering very large document datasets there is considerable ongoing interest in computational speed-ups for very large datasets, with "on-line" (sequential) approaches capable of dealing with millions of documents [47] that could be useful in the future for very large RNA-seq datasets.

A thorny issue that arises when fitting these types of model is how to select the number of clusters, K. Like many software packages for fitting these models, the `maptpx` package implements a measure of model fit that provides one useful guide. However, it is worth remembering that in practice there is unlikely to be a "true" value of K, and results from different values of K may complement one another rather than merely competing with one another. For example, seeing how the fitted model evolves as K increases is one way to capture some notion of hierarchy in the clusters identified [15]. More generally it is often fruitful to analyse data in multiple ways using the same tool: for example our GTEx analyses

bioRxiv preprint doi: https://doi.org/10.1101/051631; this version posted May 4, 2016. The copyright holder for this preprint (which was not certified by peer review) is the author/funder, who has granted bioRxiv a license to display the preprint in perpetuity. It is made available under aCC-BY-NC-ND 4.0 International license.

illustrate how analysis of subsets of the data (in this case the brain samples) can complement analyses of the entire data.

The version of the GoM model fitted here is relatively simple, and could certainly be embellished. For example, the model allows the expression of each gene in each cluster to be a free parameter, whereas we might expect expression of most genes to be "similar" across clusters. This is analogous to the idea in population genetics applications that allele frequencies in different populations may be similar to one another [18], or in document clustering applications that most words may not differ appreciably in frequency in different topics. In population genetics applications incorporating this idea into the model, by using a correlated prior distribution on these frequencies, can help improve identification of subtle structure [18] and we would expect the same to happen here for RNA-seq data.

5 Methods and Materials

5.1 Model Fitting

We use the `maptpx` R package [13] to fit the GoM model (1,2), which is also known as "Latent Dirichlet Allocation" (LDA). The `maptpx` package fits this model using an EM algorithm to perform Maximum a posteriori (MAP) estimation of the parameters q and θ. See [13] for details.

5.2 Visualizing Results

In addition to the Structure plot, we have also found it useful to visualize results using t-distributed Stochastic Neighbor Embedding (t-SNE), which is a method for visualizing high dimensional datasets by placing them in a two dimensional space, attempting to preserve the relative distance between nearby samples [20, 21]. Compared with the Structure plot our t-SNE plots contain less information, but can better emphasise clustering of samples that have similar membership proportions in many clusters. Specifically, t-SNE tends to place samples with similar membership proportions together in the two-dimensional plot, forming visual "clusters" that can be identified by eye (e.g. `http://stephenslab.github.io/count-clustering/project/src/tissues_tSNE_2.html`). This may be particularly helpful in settings where no external information is available to aid in making an informative Structure plot.

5.3 Cluster annotation

To help biologically interpret the clusters, we developed a method to identify which genes are most distinctively differentially expressed in each cluster. (This is analogous to identifying "ancestry informative markers" in population genetics applications [16].) Specifically, for each cluster k we measure the distinctiveness of gene g with respect to any other cluster l using

$$\mathrm{KL}^g[k,l] := \theta_{kg}\, log\frac{\theta_{kg}}{\theta_{lg}} + \theta_{lg} - \theta_{kg}, \tag{3}$$

bioRxiv preprint doi: https://doi.org/10.1101/051631; this version posted May 4, 2016. The copyright holder for this preprint (which was not certified by peer review) is the author/funder, who has granted bioRxiv a license to display the preprint in perpetuity. It is made available under aCC-BY-NC-ND 4.0 International license.

which is the Kullback–Leibler divergence of the Poisson distribution with parameter θ_{kg} to the Poisson distribution with parameter θ_{lg}. For each cluster k, we then define the distinctiveness of gene g as

$$D^g[k] = \min_{l \neq k} \mathrm{KL}^g[k, l]. \tag{4}$$

The higher $D^g[k]$, the larger the role of gene g in distinguishing cluster k from all other clusters. Thus, for each cluster k we identify the genes with highest $D^g[k]$ as the genes driving the cluster k. We annotate the biological functions of these individual genes using the `mygene` R Bioconductor package [28].

For each cluster k, we filter out a number of genes (top 100 for the Deng *et al* data [23] and GTEx V6 data [11]) with highest $D^g[k]$ value and perform a gene set over-representation analysis of these genes against all the other genes in the data representing the background. To do this, we used ConsensusPathDB database (`http://cpdb.molgen.mpg.de/`) [48] [49]. See Table 1-2 and Table 3 for the top significant gene ontologies driving each cluster in the GTEx V6 data and the Deng *et al* data respectively.

5.4 Comparison with hierarchical clustering

We compared the GoM model with a distance-based hierarchical clustering algorithm by applying both methods to samples from pairs of tissues from the GTEx project, and assessed their accuracy in separating samples according to tissue. For each pair of tissues we randomly selected 50 samples from the pool of all samples coming from these tissues. For the hierarchical clustering approach we cut the dendogram at $K = 2$, and checked whether or not this cut partitions the samples into the two tissue groups. (We applied hierarchical clustering using Euclidean distance, with both complete and average linkage; results were similar and so we showed results only for complete linkage.)

For the GoM model we analysed the data with $K = 2$, and sorted the samples by their membership in cluster 1. We then partitioned the samples at the point of the steepest fall in this membership, and again we checked whether this cut partitions the samples into the two tissue groups.

Fig 2 shows, for each pair of tissues, whether each method successfully partitioned the samples into the two tissue groups.

5.5 Thinning

We used "thinning" to simulate lower-coverage data from the original higher-coverage data.. Specifically, if c_{ng} is the counts of number of reads mapping to gene g for sample n for the original data, we simulated thinned counts t_{ng} using

$$t_{ng} \sim Bin(c_{ng}, p_{thin}) \tag{5}$$

where p_{thin} is a specified thinning parameter.

bioRxiv preprint doi: https://doi.org/10.1101/051631; this version posted May 4, 2016. The copyright holder for this preprint (which was not certified by peer review) is the author/funder, who has granted bioRxiv a license to display the preprint in perpetuity. It is made available under aCC-BY-NC-ND 4.0 International license.

5.6 Code Availability

Our methods are implemented in an R package `CountClust`, available as part of the Bioconductor project at `https://www.bioconductor.org/packages/3.3/bioc/html/CountClust.html`. The development version of the package is also available at `https://github.com/kkdey/CountClust`.

Code for reproducing results reported here is available at `http://stephenslab.github.io/count-clustering/`.

Acknowledgements

The Genotype-Tissue Expression (GTEx) Project was supported by the Common Fund of the Office of the Director of the National Institutes of Health. Additional funds were provided by the NCI, NHGRI, NHLBI, NIDA, NIMH, and NINDS. Donors were enrolled at Biospecimen Source Sites funded by NCI SAIC-Frederick, Inc. (SAIC-F) subcontracts to the National Disease Research Interchange (10XS170), Roswell Park Cancer Institute (10XS171), and Science Care, Inc. (X10S172). The Laboratory, Data Analysis, and Coordinating Center (LDACC) was funded through a contract (HHSN268201000029C) to The Broad Institute, Inc. Biorepository operations were funded through an SAIC-F subcontract to Van Andel Institute (10ST1035). Additional data repository and project management were provided by SAIC-F (HHSN261200800001E). The Brain Bank was supported by a supplements to University of Miami grants DA006227 & DA033684 and to contract N01MH000028. Statistical Methods development grants were made to the University of Geneva (MH090941 & MH101814), the University of Chicago (MH090951, MH090937, MH101820, MH101825), the University of North Carolina - Chapel Hill (MH090936 & MH101819), Harvard University (MH090948), Stanford University (MH101782), Washington University St Louis (MH101810), and the University of Pennsylvania (MH101822). The data used for the analyses described in this manuscript were obtained from: the GTEx Portal on 10/19/2015 and dbGaP accession number phs000424.v6.p1.

The paper is supported by the grant U01CA198933 from the NIH BD2K program.

We thank Matt Taddy, Amos Tanay and Effi Kenigsberg for helpful discussions. We thank Po-Yuan Tung, John Blischak and Jonathan Pritchard for helpful comments on the draft manuscript.

Disclosure Declaration

The authors have no conflict of interest.

bioRxiv preprint doi: https://doi.org/10.1101/051631; this version posted May 4, 2016. The copyright holder for this preprint (which was not certified by peer review) is the author/funder, who has granted bioRxiv a license to display the preprint in perpetuity. It is made available under aCC-BY-NC-ND 4.0 International license.

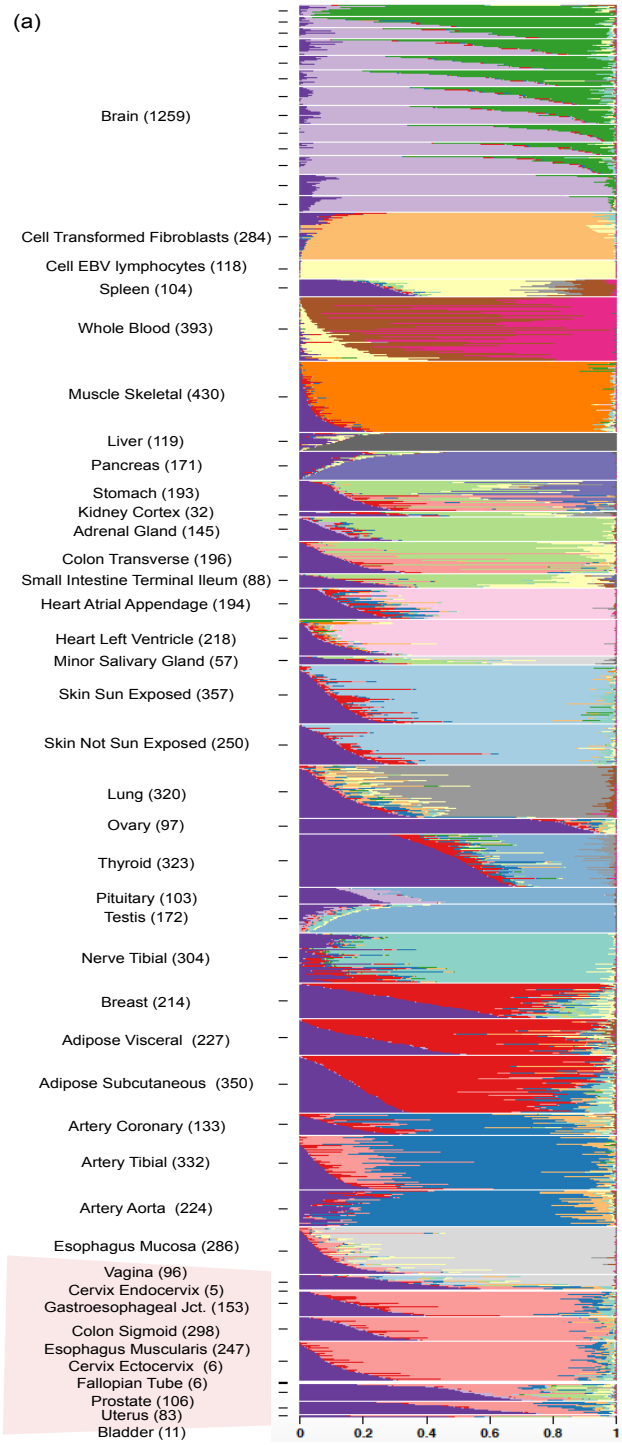

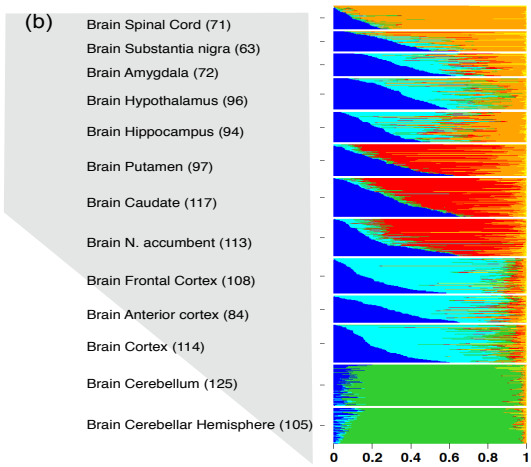

(a) clusters	Top 5 driving genes
1 : Royal Purple	*NEAT1, IGFBP5, CCLN2, SRSF5, PNISR*
2 : Light purple	*SNAP25, FBXL16, NCDN, SNCB, SLC17A7*
3 : Red	*FABP4, PLIN1, FASN, GPX3, LIPE*
4 : Salmon	*ACTG2, MYH11, SYNM, MYLK, CSRP1*
5 : Denim	*RGS5, MGP, AEBP1, IGFBP7, MFGE5*
6 : Light denim	*KRT10, KRT1, KRT2, LOR, KRT14*
7 : Orange	*NEB, MYH1, MYH2, MYBPC1, ACTA1*
8 : Light orange	*FN1, COL1A1, COL1A2, COL3A1, COL6A3*
9 : Green	*MBP, GFAP, MTURN, H1PK2, CARNS1*
10 : Light green	*CYP17A1, CYP11B1, PIGR, GKN1, STAR*
11 : Turquoise	*MPZ, APOD, PMP22, PRX, NGFR*
12 : Yellow	*IGHM, IGHG1, IGHG2, IGHG4, CD74*
13 : Sky blue	*TG, PRL, GH1, PRM2, PRM1*
14 : Light pink	*NPPA, MYH6, TNNT2, ACTC1, MYBPC3*
15 : Light gray	*KRT13, KRT4, MUC7, CRNN, KRT6A*
16 : Gray	*SFTPB, SFTPA1, SFTPA2, SFTPC, A2M*
17 : Brown	*CSF3R, MMP25, IL1R2, SELL, VNN2*
18 : Purple	*PRSS1, CPA1, PNLIP, CELA3A, GP2*
19 : Pink	*HBB, HBA2, HBA1, FKBP8, HBD*
20 : Dark gray	*ALB, HP, FGB, FGA, ORM1*

(b) clusters	Top 5 driving genes
1 : Royal blue	*CLU, OXT, GLUL, NDRG2, CST3*
2 : Turquoise	*ENC1, NCALD, YWHAH, KIF5A, NPTXR*
3 : Lime green	*PKD1, CBLN3, CHGB, COL27A1, ABLIM1*
4 : Bright red	*PPP1R1B, RGS14, NCDN, PDE1B, RAP1GAP*
5 : Yellow orange	*MBP, GFAP, TF, MTURN, SCD*
6 : Yellow	*IQGAP1, A2M, C3, MYH7, TG*

Fig 1. (a): Structure plot of estimated membership proportions for GoM model with $K = 20$ clusters fit to 8555 tissue samples from 53 tissues in GTEx data. Each horizontal bar shows the cluster membership proportions for a single sample, ordered so that samples from the same tissue are adjacent to one another. Within each tissue, the samples are sorted by the proportional representation of the underlying clusters.**(b)**: Structure plot of estimated membership proportions for $K = 4$ clusters fit to only the brain tissue samples. This analysis highlights finer-scale structure among the brain samples that is missed by the global analysis in (a).

bioRxiv preprint doi: https://doi.org/10.1101/051631; this version posted May 4, 2016. The copyright holder for this preprint (which was not certified by peer review) is the author/funder, who has granted bioRxiv a license to display the preprint in perpetuity. It is made available under aCC-BY-NC-ND 4.0 International license.

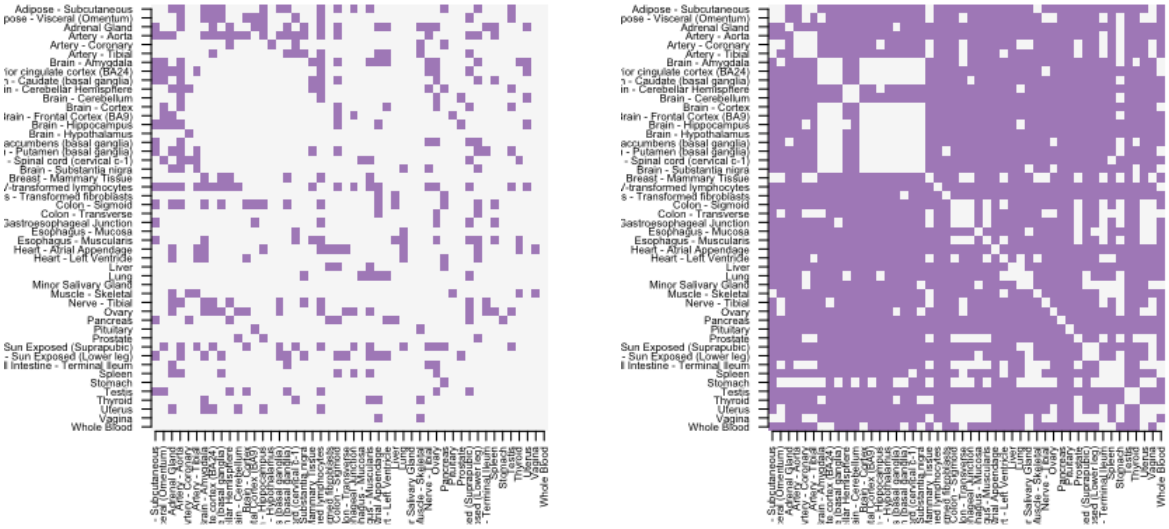

(a) hierarchy method **(b)** GoM method

Fig 2. A comparison of accuracy of GoM model vs hierarchical clustering. For each pair of tissues from the GTEX data we assessed whether or not each method (with $K = 2$ clusters) separated the samples precisely according to their actual tissue of origin, with successful separation indicated by a filled square. Some pairs of tissues (e.g. pairs of brain tissues) are more difficult to distinguish than others. Overall the GoM model is successful in 86% comparisons and the hierarchical clustering in 39% comparisons.

bioRxiv preprint doi: https://doi.org/10.1101/051631; this version posted May 4, 2016. The copyright holder for this preprint (which was not certified by peer review) is the author/funder, who has granted bioRxiv a license to display the preprint in perpetuity. It is made available under aCC-BY-NC-ND 4.0 International license.

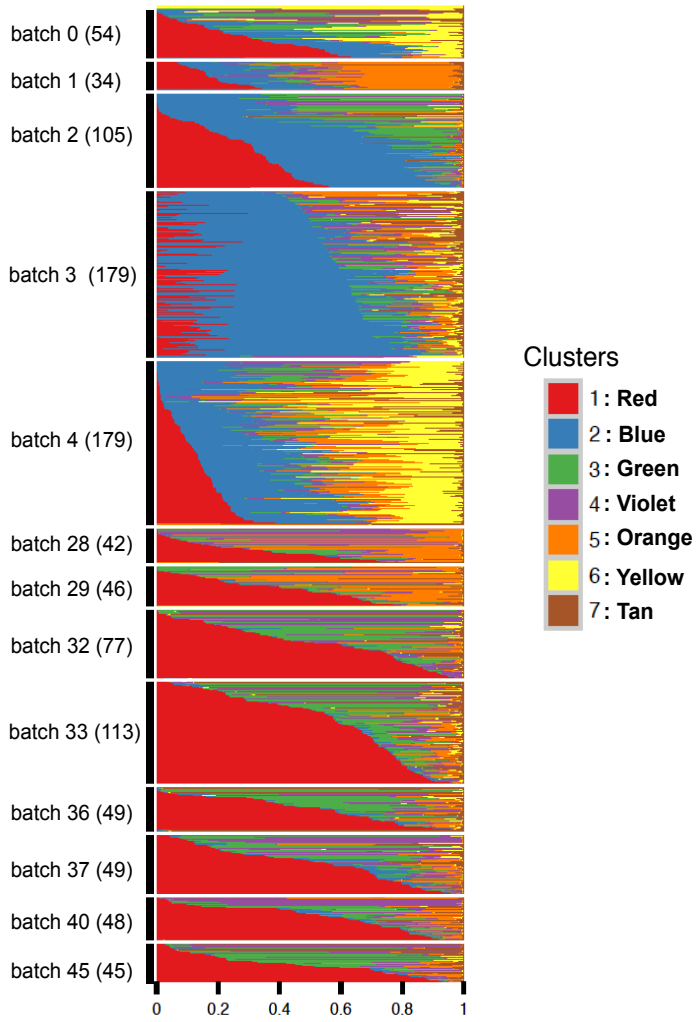

Fig 3. Structure plot of estimated membership proportions for GoM model with $K = 7$ clusters fit to $1,041$ single cells from [22]. The samples (cells) are ordered so that samples from the same amplification batch are adjacent and within each batch, the samples are sorted by the proportional representation of the underlying clusters. In this analysis the samples do not appear to form clearly-defined clusters, with each sample being allocated membership in several "clusters". Membership proportions are correlated with batch, and some groups of batches (e.g. 28-29; 32-45) show similar palettes. These results suggest that batch effects are likely influencing the inferred structure in these data.

bioRxiv preprint doi: https://doi.org/10.1101/051631; this version posted May 4, 2016. The copyright holder for this preprint (which was not certified by peer review) is the author/funder, who has granted bioRxiv a license to display the preprint in perpetuity. It is made available under aCC-BY-NC-ND 4.0 International license.

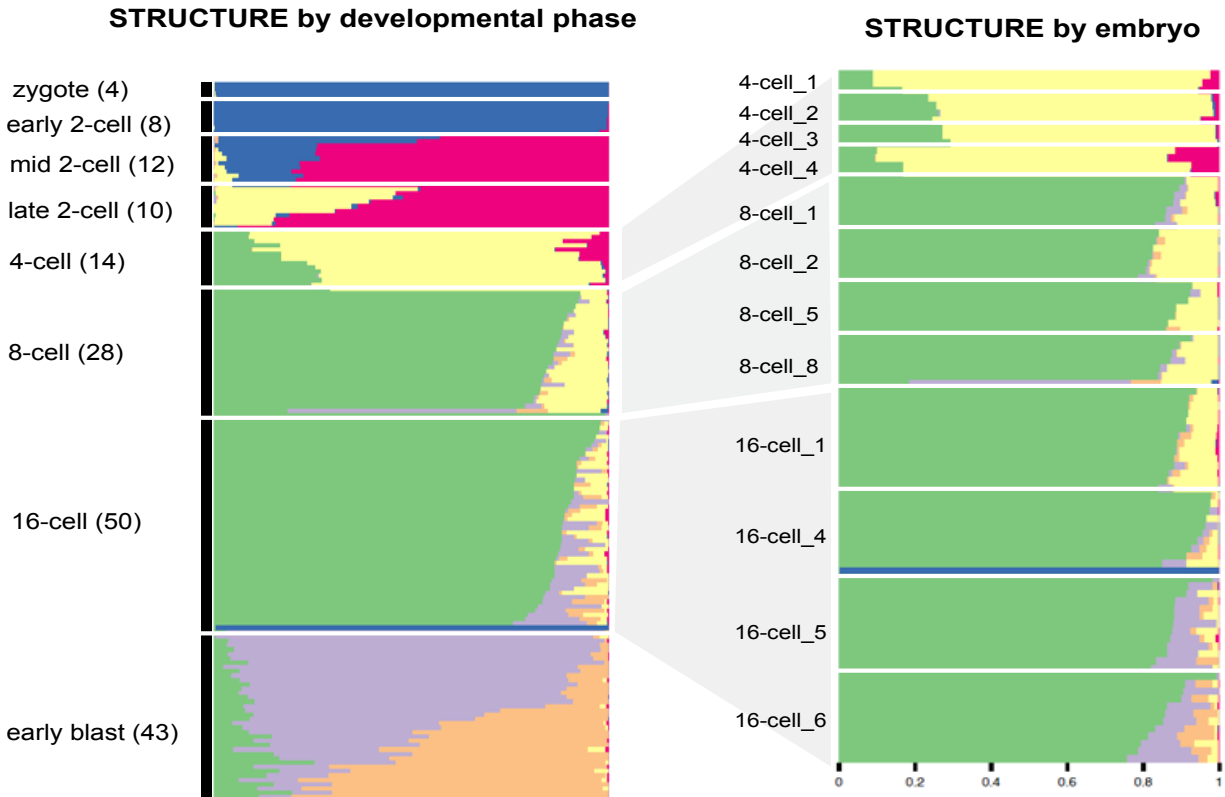

Clusters	Top 5 driving genes	GO annotations summary
1: Blue	*Bcl2l10, Tcl1 , E330034G19RiK, LOC100502936, Oas1d*	*Gamete generation, Oocyte development & differentiation, Cell devision regulation*
2: Magenta	*Obox3, Zfp352, Gm8300, Usp17l5, BB287469*	*Nuclear body, Centriole, Microtubule organizing center part*
3: Yellow	*Rtn2, Ebna1bp2, Zfp259, Nasp, Cenpe*	*Nuclear part, Nuclear lumen, Intracellular organelle, Nucleolus, Microtubule*
4: Green	*Timd2, Isyna1, Alppl2, Prame15, Hsp90Ab1*	*Cytosol, Cytoplasmic Part, Catabolic Process, Protein Binding, Ubiquitin Ligase*
5: Purple	*Upp1, Tdgf1, Aqp8, Fabp5, Tat*	*Extracellular Exosome/Vesicle/Organelle, Metabolic Process, Blood Vessel Morphogenesis*
6: Orange	*Actb, Krt18, Fabp3, Id2, Tspan8*	*Extracellular Exome/Organelle, Membrane Bound Organelle, Actin Cytoskeleton, Actin Filament Bundle*

Fig 4. Structure plot of estimated membership proportions for GoM model with $K = 6$ clusters fit to 259 single cells from [23]. The cells are ordered by their preimplantation development phase (and within each phase, sorted by the proportional representation of the clusters). While the very earliest developmental phases (zygote and early 2-cell) are essentially assigned to a single cluster, others have membership in multiple clusters. Each cluster is annotated by the genes that are most distinctively expressed in that cluster, and by the gene ontology categories for which these distinctive genes are most enriched (see Table 3 for more extensive annotation results). See text for discussion of biological processes driving these results.

bioRxiv preprint doi: https://doi.org/10.1101/051631; this version posted May 4, 2016. The copyright holder for this preprint (which was not certified by peer review) is the author/funder, who has granted bioRxiv a license to display the preprint in perpetuity. It is made available under aCC-BY-NC-ND 4.0 International license.

Table 1. Cluster Annotations GTEx V6 data (with GO annotations).

Cluster	Top 5 Driving Genes	Top significant GO terms
1. Royal purple	*NEAT1, IGFBP5, CCLN2, SRSF5, PNISR*	GO:0005654 (nucleoplasm), GO:0044428 (nuclear part), GO:0044822 (poly-A RNA binding), GO:0043233 (organelle lumen)
2. Light purple	*SNAP25, FBXL16, NCDN, SNCB, SLC17A7*	GO:0097458 (neuron part), GO:0007268 (synaptic transmission), GO:0030182 (neuron differentiation), GO:0022008 (neurogenesis), GO:0007267 (cell-cell signaling)
3. Red	*FABP4, PLIN1, FASN, GPX3, LIPE*	GO:0044255 (cellular lipid metabolism), GO:0006629 (lipid metabolism), GO:0006639 (acylglycerol metabolism), GO:0045765 (angiogenesis regulation), GO:0019915 (lipid storage)
4. Salmon	*ACTG2, MYH11, SYNM, MYLK, CSRP1*	GO:0043292 (contractile fiber), GO:0006936 (muscle contraction), GO:0015629 (actin cytoskeleton), GO:0030016 (myofibril), GO:0005925 (focal adhesion)
5. Denim	*RGS5, MGP, AEBP1, IGFBP7, MFGE8*	GO:0005578 (proteinaceous extracellular matrix), GO:0030198 (extracellular matrix), GO:0007155 (cell adhesion), GO:0001568 (blood vessel development)
6. Light denim	*KRT10, KRT1, KRT2, LOR, KRT14*	GO:0008544 (epidermis development), GO:0043588 (skin development), GO:0042303 (molting cycle), GO:0042633 (hair cycle), GO:0048513 (organ development
7. Orange	*NEB, MYH1, MYH2, MYBPC1, ACTA1*	GO:0043292 (contractile fiber), GO:0030016 (myofibril), GO:0030017 (sarcomere), GO:0003012 (muscle system process), GO:0015629 (actin cytoskeleton)
8. Light orange	*FN1, COL1A1, COL1A2, COL3A1, COL6A3*	GO:0030198 (extracellular matrix), GO:0043062 (extracellular structure), GO:0032963 (collagen metabolism), GO:0030199 (collagen fibril organization), GO:0030574 (collagen catabolism)
9. Green	*MBP, GFAP, MTURN, HIPK2, CARNS1*	GO:0043209 (myelin sheath), GO:0007399 (nervous system development), GO:0008366 (axon ensheathment), GO:0044430 (cytoskeletal part), GO:0005874 (microtubule)
10. Light green	*CYP17A1, CYP11B1, PIGR, GKN1, STAR*	GO:0006694 (steroid biosynthesis), GO:0008202 (steroid metabolism), GO:0016125 (sterol metabolism), GO:0042446 (hormone biosynthesis), GO:0008207 (C21-steroid hormone metabolism)
11. Turquoise	*MPZ, APOD, PMP22, PRX, NGFR*	GO:0008366 (axon ensheathment), GO:0048856 (anatomical structure development), GO:0007272 (ensheathment of neurons), GO:0042552 (myelination), GO:0005578 (proteinaceous extracellular matrix)
12. Yellow	*IGHM, IGHG1, IGHG2, IGHG4, CD74*	GO:0006955 (immune response), GO:0002252 (immune effector process), GO:0003823 (antigen binding), GO:0019724 (B-cell mediated immunity), GO:0002684 (positive regulation immune system)
13. Sky blue	*TG, PRL, GH1, PRM2, PRM1*	GO:0019953 (sexual reproduction), GO:0048232 (male gamete generation), GO:0035686 (sperm fibrous sheath), GO:0005179 (hormone activity), GO:0042403 (thyroid hormone metabolism)
14. Light pink	*NPPA, MYH6, TNNT2, ACTC1, MYBPC3*	GO:0045333 (cellular respiration), GO:0022904 (respiratory electron transport), GO:0031966 (mitochondrial membrane), GO:0015980 (energy derivation by oxidation of organic compounds)
15. Light gray	*KRT13, KRT4, MUC7, CRNN, KRT6A*	GO:0043230 (extracellular organelle), GO:0070062 (extracellular exosome), GO:0031982 (vesicle), GO:0008544 (epidermis development), GO:0043588 (skin development)
16. Gray	*SFTPBß, SFTPA1, SFTPA2, SFTPC, A2M*	GO:0001525 (angiogenesis), GO:0048514 (blood vessel morphogenesis), GO:2000145 (cell motility regulation), GO:0071944 (cell periphery), GO:0009611 (response to wounding)
17. Brown	*CSF3R, MMP25, IL1R2, SELL, VNN2*	GO:0006955 (immune response), GO:0006952 (defense response), GO:0071944 (cell periphery), GO:0005886 (plasma membrane), GO:0050776 (regulation of immune response)
18. Purple	*PRSS1, CPA1, PNLIP, CELA3A, GP2*	GO:0007586 (digestion), GO:0004252 (serine-type endopeptidase activity), GO:0006508 (proteolysis), GO:0044241 (lipid digestion), GO:0016787 (hydrolase activity)
19. Pink	*HBB, HBA2, HBA1, FKBP8, HBD*	GO:0005833 (hemoglobin complex), GO:0015669 (gas transport), GO:0020037 (heme binding), GO:0031720 (haptoglobin binding), GO:0006950 (response to stress)
20. Dark gray	*ALB, HP, FGB, FGA, ORM1*	GO:0034364 (high density lipoprotein), GO:0019752 (carboxylic acid metabolism), GO:0044710 (single organism metabolism), GO:0002526 (acute inflammatory response), GO:0031982 (vesicle)

bioRxiv preprint doi: https://doi.org/10.1101/051631; this version posted May 4, 2016. The copyright holder for this preprint (which was not certified by peer review) is the author/funder, who has granted bioRxiv a license to display the preprint in perpetuity. It is made available under aCC-BY-NC-ND 4.0 International license.

Table 2. Cluster Annotations for GTEx V6 Brain data.

Cluster	Top 5 Driving Genes	Top significant GO terms
1. Royal blue	*CLU, OXT, GLUL, NDRG2, CST3*	GO:0043230 (extracellular organelle), GO:1903561 (extracellular vesicle), GO:0070062 (extracellular exosome), GO:0006950 (response to stress), GO:0031988 (membrane bound vesicle)
2. Turquoise	*ENC1, NCALD, YWHAH, KIF5A, NPTXR*	GO:0097458 (neuron part), GO:0008092 (cytoskeletal protein binding), GO:0031175 (neuron projection development), GO:0030182 (neuron differentiation), GO:0007268 (synaptic transmission)
3. Lime green	*PKD1, CBLN3, CHGB, COL27A1, ABLIM1*	GO:0005089 (Rho guanyl-nucleotide exchange factor activity), GO:0022008 (neurogenesis), GO:0035239 (tube morphogenesis), GO:0016604 (neuron body), GO:0006836 (neurotransmitter transport)
4. Red	*PPP1R1B, RGS14, NCDN, PDE1B, RAP1GAP*	GO:0065009 (regulation of molecular function), GO:0036477 (somatodendritic compartment), GO:0007268 (synaptic transmission), GO:0023051 (signaling regulation), GO:0010646 (cell communication regulation)
5. Yellow orange	*MBP, GFAP, TF, MTURN, SCD*	GO:0043209 (myelin sheath), GO:0007399 (nervous system development), GO:0007272 (ensheathment of neurons), GO:0048471 (perinuclear region of cytoplasm), GO:0010646 (cell communication regulation)
6. Yellow	*IQGAP1, A2M, C3, MYH7, TG*	GO:0072562 (blood microparticle), GO:0044449 (contractile fiber part), GO:0043230 (extracellular organelle), GO:0030017 (sarcomere), GO:0072376 (protein activation cascade)

Table 3. Cluster Annotations for Deng et al (2014) data.

Cluster	Top 10 Driving Genes	Top significant GO terms
1. Blue	*Bcl2l10*, *E330034G19Rik*, *Tcl1*,*LOC100502936*, *Oas1d*, *AU022751*, *Spin1*, *Khdc1b*, *D6Ertd527e*, *Btg4*	GO:0007276 (gamete generation), GO:0032504 (multicellular organism reproduction), GO:0044702 (single organism reproduction), GO:0048477 (oogenesis), GO:0048599 (oocyte development), GO:0009994 (oocyte differentiation), GO:0051321 (meiotic cell cycle), GO:0006306 (DNA methylation), GO:0051302 (regulation of cell division)
2. Magenta	*Obox3*, *Zfp352*, *Gm8300*, *Usp17l5*, *BB287469*, *Rfpl4b*, *Gm2022*, *Gm5662*, *Gm11544* , *Gm4850*	GO:0016604 (nuclear body), GO:0005814 (centriole), GO:0044450 (microtubule organizing center part)
3. Yellow	*Rtn2*, *Ebna1bp2*, *Zfp259*, *Nasp*, *Cenpe*, *Rnf216*, *Ctsl*, *Tor1b*, *Ankrd10*, *Lamp2*	GO:0044428 (nuclear part), GO:0031981 (nuclear lumen), GO:0070013 (intracellular organelle lumen), GO:0005730 (nucleolus), GO:0005654 (nucleoplasm), GO:0003723 (RNA binding), GO:0005874 (microtubule), GO:0043229 (intracellular organelle)
4. Green	*Timd2*, *Isyna1*, *Alppl2*, *Prame15*, *Fbxo15*, *Tceb1*, *Gpd1l*, *Pemt*, *Hsp90aa1*, *Hsp90ab1*	GO:0005829 (cytosol), GO:0044444 (cytoplasmic part), GO:1901575 (organic substance catabolic process), GO:0000151 (ubiquitin ligase com- plex), GO:0009056 (catabolic process), GO:0072655 (protein localization mitochondrion), GO:0044265 (cellular macromolecule catabolic process), GO:0051082 (unfolded protein binding), GO:0023026 (MHC class II protein complex binding), GO:0055131 (C3HC4-type RING finger domain binding)
5. Purple	*Upp1*, *Tdgf1*, *Aqp8*, *Fabp5*, *Tat*, *Pdgfra*, *Pyy*, *Prdx1*, *Col4a1*, *Spp1*	GO:0070062 (extracellular exosome), GO:0043230 (extracellular organelle), GO:1903561 (extracellular vesicle), GO:0006950 (response to stress), GO:0006979 (response to oxidative stress), GO:0044710 (metabolic process), GO:0048514 (blood vessel morphogenesis), GO:0001944 (vasculature development), GO:0030198 (extracellular matrix organization)
6. Orange	*Actb*, *Krt18*, *Fabp3*, *Id2*, *Tspan8*, *Gm2a*, *Lgals1*, *Adh1* , *Lrp2*, *BC051665*	GO:0065010 (extracellular membrane-bounded organelle), GO:0070062 (extracellular exosome), GO:0043230 (extracellular organelle), GO:1903561 (extracellular vesicle), GO:0031982 (vesicle), GO:0048468 (cell development), GO:0030036 (actin cytoskeleton and organization), GO:0032432 (actin filament bundle), GO:0005912 (adherens junction)

bioRxiv preprint doi: https://doi.org/10.1101/051631; this version posted May 4, 2016. The copyright holder for this preprint (which was not certified by peer review) is the author/funder, who has granted bioRxiv a license to display the preprint in perpetuity. It is made available under aCC-BY-NC-ND 4.0 International license.

References

1. Hernandez MC , Andres-Barquin PJ , Martinez S , Bulfone A , Rubenstein JL , Israel MA. 1997. ENC-1: a novel mammalian kelch-related gene specifically expressed in the nervous system encodes an actin-binding protein. *J Neurosci.*,17(9): 3038-51.
2. Baba H, Nakahira K, Morita N, Tanaka F, Akita H, Ikenaka K. GFAP gene expression during development of astrocyte. *Dev Neurosci.*, 19(1):49-57.
3. Eisen MB, Spellman PT, Brown PO and Botstein D. 1998. Cluster analysis and display of genome-wide expression patterns. *PNAS*, 95(25): 14863-14868
4. Golub TR, Slonim DK, Tamayo P, Huard C, Gaasenbeek M, Mesirov JP, Coller H, Loh ML, Downing JR, Caligiuri MA, Bloomfield CD, Lander ES. 1999. Molecular classification of cancer: class discovery and class prediction by gene expression monitoring. *Science*, 286(5439): 531-7
5. Alizadeh AA1, Eisen MB, Davis RE, Ma C, Lossos IS, Rosenwald A, Boldrick JC *et al.* 2000. Distinct types of diffuse large B-cell lymphoma identified by gene expression profiling. *Nature*, 403(6769): 503-11
6. D'haeseleer P. 2005. How does gene expression clustering work? *Nat Biotechnol*, 23(12):1499-501
7. Jiang D, Tang C, Zhang A. Cluster Analysis for Gene Expression Data: A Survey. *Microsoft Research*, http://research.microsoft.com/en-us/people/djiang/tkde04.pdf.
8. Erosheva EA. 2006. Latent class representation of the grade of membership model. Seattle: University of Washington.
9. Tang F, Barbacioru C, Wang Y, Nordman E, Lee C et al. 2009. mRNA-Seq whole-transcriptome analysis of a single cell. *Nature Methods*, 6, 377 - 382.
10. Trapnell C. 2015. Defining cell types and states with single-cell genomics. *Genome Res.*, 25, 1491-1498.
11. The GTEx Consortium. 2013. The Genotype-Tissue Expression (GTEx) project. *Nature genetics.* 45(6): 580-585. doi:10.1038/ng.2653.
12. Oshlack A, Robinsom MD, Young MD. 2010. From RNA-seq reads to differential expression results. *Genome Biology.* 11:220, DOI: 10.1186/gb-2010-11-12-220
13. Matt Taddy. 2012. On Estimation and Selection for Topic Models. *AISTATS 2012, JMLR W&CP 22.* (maptpx R package).
14. Pritchard, Jonathan K., Matthew Stephens, and Peter Donnelly. 2000. Inference of population structure using multilocus genotype data. *Genetics.* 155.2, 945-959.
15. Rosenberg NA, Pritchard JK, Weber JL, Cann HM, Kidd KK, Zhivotovsky LA, Feldman MW. 2002. The genetic structure of human populations. *Science.* 298, 2381-2385.
16. Rosenberg NA. 2005. Algorithms for selecting informative marker panels for population assignment. *J Comput Biol.* 12(9), 1183-201.
17. Raj A, Stephens M, Pritchard JK. 2014. fastSTRUCTURE: Variational Inference of Population Structure in Large SNP Data Sets. *Genetics.* 197, 573-589.
18. Falush D, Stephens M, Pritchard JK. 2003. Inference of population structure using multilocus genotype data: linked loci and correlated allele frequencies. *Genetics.* 164(4), 1567-87.
19. Engelhardt BE, Stephens M. 2010. Analysis of Population Structure: A Unifying Framework and Novel Methods Based on Sparse Factor Analysis. *PLOS Genetics.* DOI: 10.1371/journal.pgen.1001117.
20. van der Maaten LJP and Hinton GE. 2008. Visualizing High-Dimensional Data Using t-SNE. *J. Mach. Learn. Res..* 2579-2605.
21. L.J.P. van der Maaten. 2014. Accelerating t-SNE using Tree-Based Algorithms. *J. Mach. Learn. Res..* 3221-3245.
22. Jaitin DA, Kenigsberg E et al. 2014. Massively Parallel Single-Cell RNA-Seq for Marker-Free Decomposition of Tissues into Cell Types. *Science.* 343 (6172) 776-779.
23. Deng Q, Ramskold D, Reinius B, Sandberg R. 2014. Single-Cell RNA-Seq Reveals Dynamic, Random Monoallelic Gene Expression in Mammalian Cells. *Science.* 343 (6167) 193-196.
24. Leek JT, Storey JD. 2007. Capturing Heterogeneity in Gene Expression Studies by Surrogate Variable Analysis *PLoS Genet.* 3(9): e161. doi:10.1371/journal.pgen.0030161
25. Stegle O, Parts L , Piipari M, Winn J, Durbin R. 2012. Using probabilistic estimation of expression residuals (PEER) to obtain increased power and interpretability of gene expression analyses. *Nat Protoc..* 7(3):500-7. doi: 10.1038/nprot.2011.457.
26. Leek JT, Scharpf RB, Bravo HC, Simcha D, Langmead B, Johnson WE, Geman D, Baggerly K, Irizarry RA. 2010. Tackling the widespread and critical impact of batch effects in high-throughput data. *Nature Reviews Genetics.* 11, 733-739.

bioRxiv preprint doi: https://doi.org/10.1101/051631; this version posted May 4, 2016. The copyright holder for this preprint (which was not certified by peer review) is the author/funder, who has granted bioRxiv a license to display the preprint in perpetuity. It is made available under aCC-BY-NC-ND 4.0 International license.

27. Hicks SC, Teng M, Irizarry RA. 2015. On the widespread and critical impact of systematic bias and batch effects in single-cell RNA-Seq data. *BiorXiv*. http://biorxiv.org/content/early/2015/09/04/025528

28. Mark A, Thompson R and Wu C. 2014. mygene: Access MyGene.Info services. *R package version 1.2.3.*.

29. Gentleman, R., Bates, D., Bolstad, B *et al*. Bioconductor: a software development project. 2003. *Technical Report, Department of Biostatistics, Harvard School of Public Health, Boston*. `https://bioconductor.org/`

30. Flutre T, Wen X, Pritchard J and Stephens M. 2013. A Statistical Framework for Joint eQTL Analysis in Multiple Tissues. *PLoS Genet*. 9(5): e1003486. doi:10.1371/journal.pgen.1003486

31. Shiraishi Y, Tremmel G, Miyano S and Stephens M. 2015. A simple model-based approach to inferring and visualizing cancer mutation signatures. *PLoS Genet*. 11(12): e1005657

32. Blei DM, Ng AY, Jordan MI. 2003. Latent Dirichlet Allocation. *J. Mach. Learn. Res.*. 3, 993-1022

33. Blei DM, Lafferty J. 2009. Topic Models. *In A. Srivastava and M. Sahami, editors, Text Mining: Classification, Clustering, and Applications . Chapman & Hall/CRC Data Mining and Knowledge Discovery Series*.

34. Shen-Orr SS, Tibshirani R, Khatri, P, Bodian DL, Staedtler F, Perry NM, Hastie, T, Sarwal MM, Davis MM, Butte AJ. 2010. Cell type specific gene expression differences in complex tissues. *Nature Methods*. 7(4), 287-289

35. Qiao W, Quon G, Csaszar E, Yu M, Morris Q, Zandstra PW. 2012. PERT: A Method for Expression Deconvolution of Human Blood Samples from Varied Microenvironmental and Developmental Conditions. *PLoS Comput Biol*. 8(12)

36. Repsilber D, Kern S, Telaar A, Walzl G, Black GF, Selbig J, Parida SK, Kaufmann SH, Jacobsen M. 2010. Biomarker discovery in heterogeneous tissue samples -taking the in-silico deconfounding approach. *BMC bioinformatics*.11(1), 27+

37. Schwartz R, Shackney SE. 2010. Applying unmixing to gene expression data for tumor phylogeny inference. *BMC bioinformatics*. 11(1), 42+

38. Lindsay J, Mandoiu I, Nelson C. 2013. Gene Expression Deconvolution using Single-cells `http://dna.engr.uconn.edu/bibtexmngr/upload/Lal.13.pdf`.

39. Wang N, Gong T, Clarke R, Chen L, Shih IeM, Zhang Z, Levine DA, Xuan J, Wang Y. 2015. UNDO: a Bioconductor R package for unsupervised deconvolution of mixed gene expressions in tumor samples. *Bioinformatics*. 31(1): 137-9

40. Ahn J, Yuan Y, Parmigiani G, Suraokar MB, Diao L, Wistuba II, Wang W. DeMix: deconvolution for mixed cancer transcriptomes using raw measured data. 2013. *Bioinformatics*. 29(15): 1865-71

41. Quon G, Haider S, Deshwar AG, Cui A, Boutros PC, Morris Q. Computational purification of individual tumor gene expression profiles leads to significant improvements in prognostic prediction. *Genome Med.*. 5(3): 29

42. Hu JG, Shi LL, Chen YJ, Xie XM, Zhang N, Zhu AY, Zheng JS, Feng YF, Zhang C, Xi J, Lu HZ. 2016. Differential effects of myelin basic protein-activated Th1 and Th2 cells on the local immune microenvironment of injured spinal cord. *Experimental Neurology*. 277, 190-201

43. duVerle D, Tsuda K. 2016. cellTree: Inference and visualisation of Single-Cell RNA-seq data as a hierarchical tree structure. *R package version 1.1.0*, `http://tsudalab.org`.

44. Dey K, Hsiao J, Stephens M. 2016. `CountClust` : Clustering and Visualizing RNA-Seq Expression Data using Grade of Membership Models. *R package version 0.99.3*, `https://www.bioconductor.org/packages/3.3/bioc/html/CountClust.html`

45. Renard M, Callewaert B, Baetens M, Campens L, MacDermot K et al. 2013. Novel MYH11 and ACTA2 mutations reveal a role for enhanced TGFβ signaling in FTAAD *Int J Cardiol*. 165(2), 314-321.

46. Gong B, Cao Z, Zheng P, Vitolo OV, Liu S, Staniszewski A, Moolman D, Zhang H, Shelanski M, Arancio O. 2006. Ubiquitin Hydrolase Uch-L1 Rescues β-Amyloid-Induced Decreases in Synaptic Function and Contextual Memory *Cell*. 126(4), 775-788

47. Hoffman MD, Blei DM, Bach F. 2010. Online learning for latent Dirichlet allocation. *Neural Information Processing Systems*.

48. Kamburov A, et al. 2013. The ConsensusPathDB interaction database: 2013 update. *Nucleic Acids Res*.

49. Pentchev K, et al. 2010. Evidence mining and novelty assessment of protein-protein interactions with the ConsensusPathDB plugin for Cytoscape. *Bioinformatics*.

50. Guo G, Huss M, Tong GQ, Wang C, Sun LL, Clarke ND, Robson P. Resolution of cell fate decisions revealed by single-cell gene expression analysis from zygote to blastocyst. *Developmental Cell*. 18(4), 675-685

51. Hou J, Charters AM, Lee SC, Zhao Y, Wu, MK, Jones SJM, Marra, MA, Hoodless PA. A systematic screen for genes expressed in definitive endoderm by Serial Analysis of Gene Expression (SAGE). *BMC Developmental Biology*. 7(92), 1-13

bioRxiv preprint doi: https://doi.org/10.1101/051631; this version posted May 4, 2016. The copyright holder for this preprint (which was not certified by peer review) is the author/funder, who has granted bioRxiv a license to display the preprint in perpetuity. It is made available under aCC-BY-NC-ND 4.0 International license.

52. Yoon S, Kim E, Kim YS, Lee H, Kim K, Bae J, Lee K. Role of Bcl2-like 10 (*Bcl2l10*) in regulating mouse oocyte maturation. *Biology of Reproduction*. 81(3), 497-506.

53. Evsikov AV, De Evsikova C. Gene expression during the oocyte-to-embryo transition in mammals. *Molecular Reproduction and Development*. 76, 805-818.

54. Rossant J. Development of the extraembryonic lineages. *Seminars in Developmental Biology*. 6(4), 237-247.

55. Falco G, Lee S, Stanghellini I, Bassey UC, Hamatani T, Ko MSH. Zscan4: a novel gene expressed exclusively in late 2-cell embryos and embryonic stem cells. *Developmental biology*. 307(2), 539-550.

56. Schaniel C, Ang YS, Ratnakumar K, Cormier C, James T, Bernstein E, Lemischka IR, Paddison PJ. Smarcc1/Baf155 couples self-renewal gene repression with changes in chromatic structure in mouse embroynic stem cells. *Stem cells*. 27(12), 2979-91.

57. Putkey FR, Cramer T, Morphew MK, Silk AD, Johnson RS, Mclntosh JR, Cleveland. Unstable Kinetochore-Microtubule capture and chromosomal instability following deletion of CENP-E. *Developmental cells*. 3(3), 351-365.

bioRxiv preprint doi: https://doi.org/10.1101/051631; this version posted May 4, 2016. The copyright holder for this preprint (which was not certified by peer review) is the author/funder, who has granted bioRxiv a license to display the preprint in perpetuity. It is made available under aCC-BY-NC-ND 4.0 International license.

6 Supplementary figures

S1 Fig. **Structure plot of all tissue samples in for (a)** $K = 5$**, (b)** $K = 10$**, (c)** $K = 15$**, (d)** $K = 20$ Some tissues form a separate cluster from the rest of the tissues from $K = 5$ onwards (for example: Whole Blood, Skin), whereas some tissues only form a distinctive subgroup only at $K = 20$ (for example: Arteries).

bioRxiv preprint doi: https://doi.org/10.1101/051631; this version posted May 4, 2016. The copyright holder for this preprint (which was not certified by peer review) is the author/funder, who has granted bioRxiv a license to display the preprint in perpetuity. It is made available under aCC-BY-NC-ND 4.0 International license.

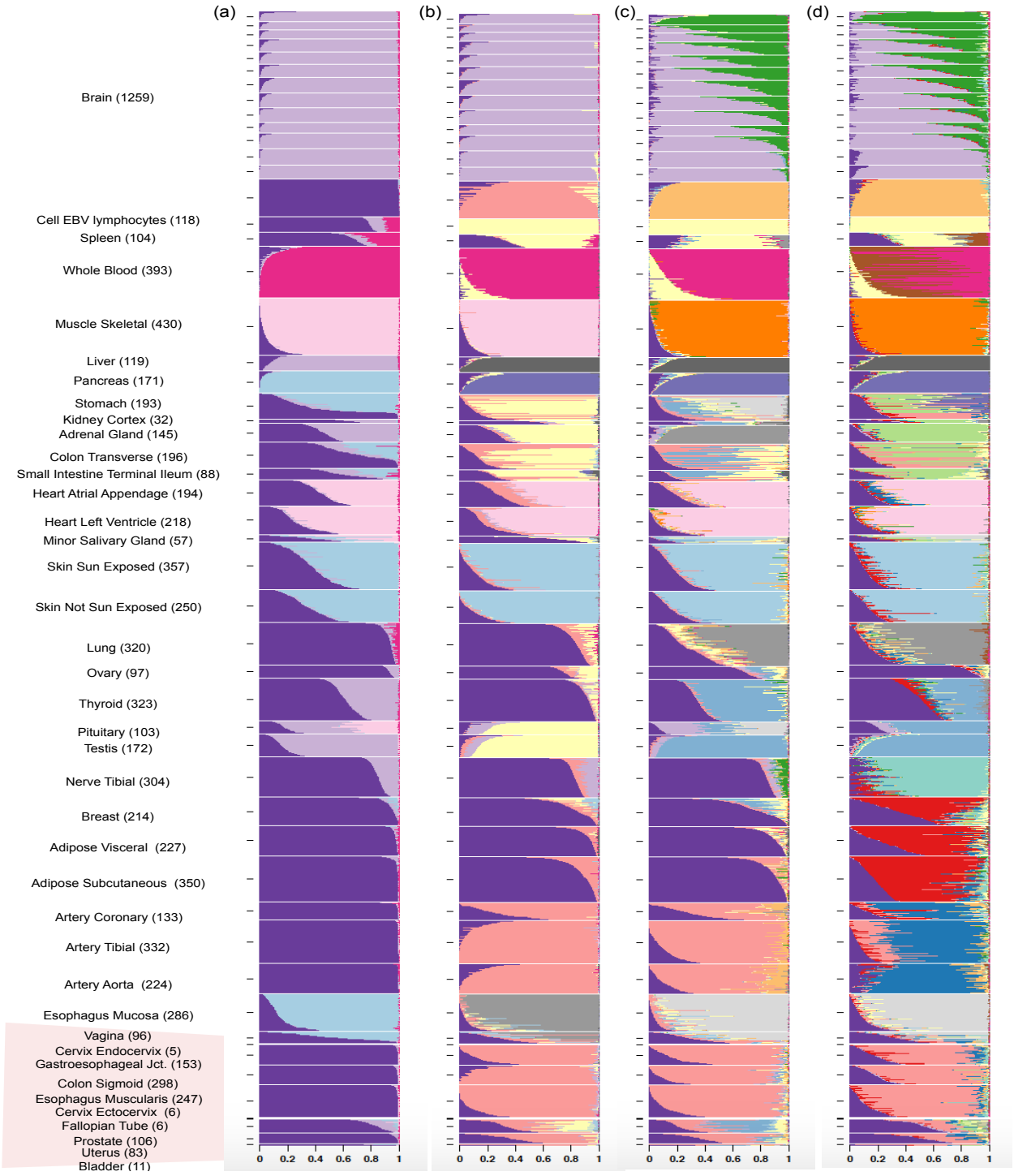

bioRxiv preprint doi: https://doi.org/10.1101/051631; this version posted May 4, 2016. The copyright holder for this preprint (which was not certified by peer review) is the author/funder, who has granted bioRxiv a license to display the preprint in perpetuity. It is made available under aCC-BY-NC-ND 4.0 International license.

S2 Fig. **Structure plot of all tissue samples in 2 runs of the GTEx V6 data for K=20 for the thinning parameters (a)** $p_{thin} = 0.01$ **and (b)** $p_{thin} = 0.0001$ The patterns in two plots closely correspond to the plot in **Fig** 1 (a), though there are a few differences from the unthinned version.

bioRxiv preprint doi: https://doi.org/10.1101/051631; this version posted May 4, 2016. The copyright holder for this preprint (which was not certified by peer review) is the author/funder, who has granted bioRxiv a license to display the preprint in perpetuity. It is made available under aCC-BY-NC-ND 4.0 International license.

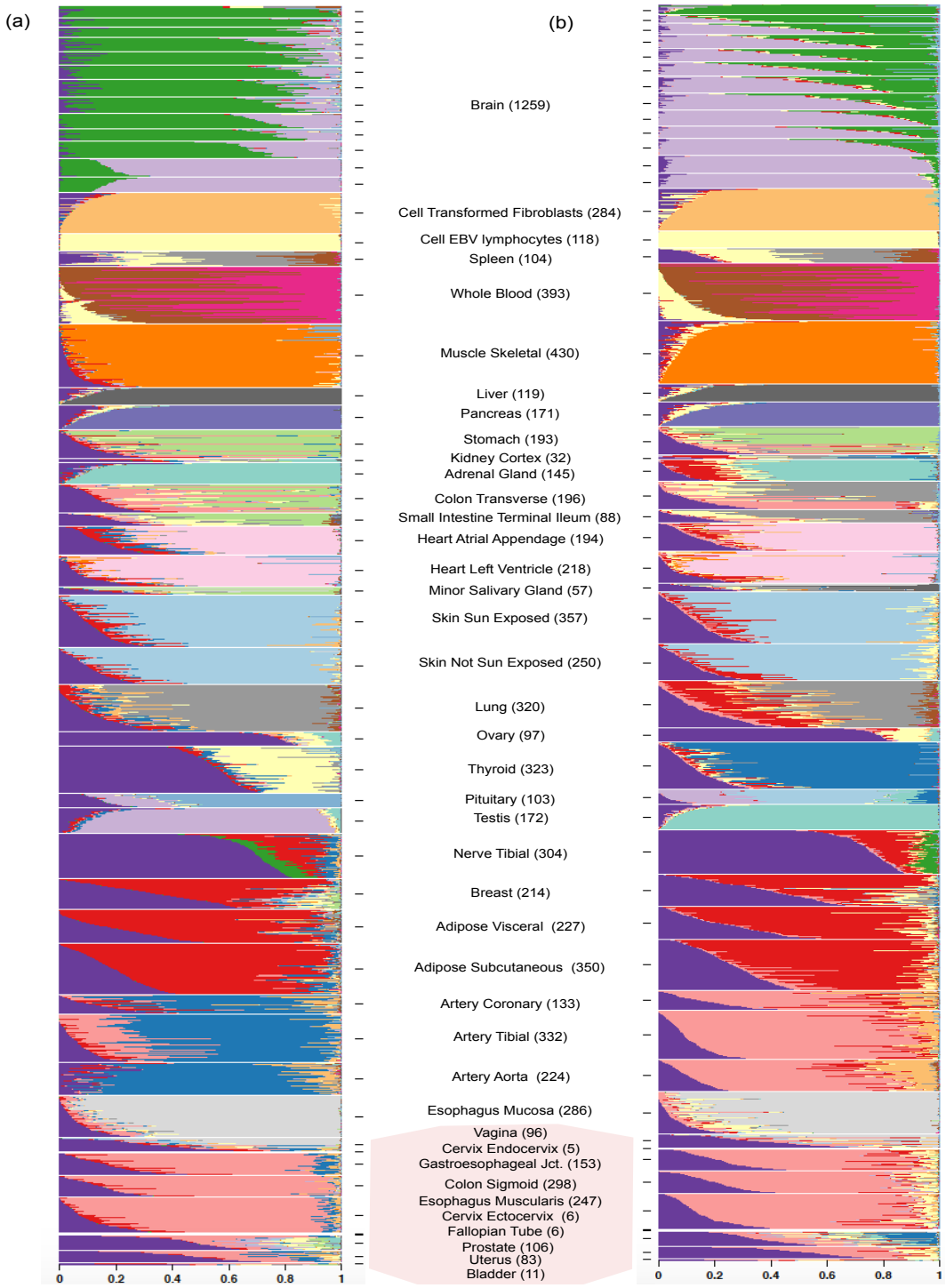

bioRxiv preprint doi: https://doi.org/10.1101/051631; this version posted May 4, 2016. The copyright holder for this preprint (which was not certified by peer review) is the author/funder, who has granted bioRxiv a license to display the preprint in perpetuity. It is made available under aCC-BY-NC-ND 4.0 International license.

S3 Fig. A comparison of "accuracy" of hierarchical vs model-based clustering on thinned GTEx data, with thinning parameter $p_{thin} = 0.01$ and $p_{thin} = 0.0001$. For each pair of tissues from the GTEx data we assessed whether or not each clustering method (with $K = 2$ clusters) separated the samples according to their actual tissue of origin, with successful separation indicated by a filled square. Thinning deteriorates accuracy compared with the unthinned data (Figure 2), but even then the model-based method remains more successful than the hierarchical clustering in separating the samples by tissue or origin.

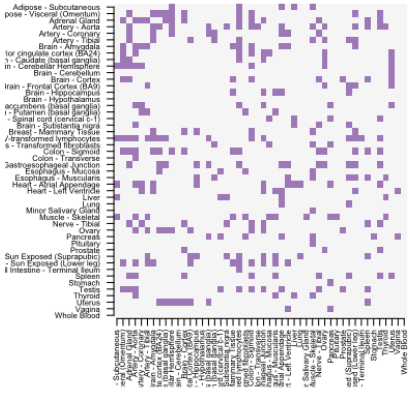

(a) hierarchy thin 0.01

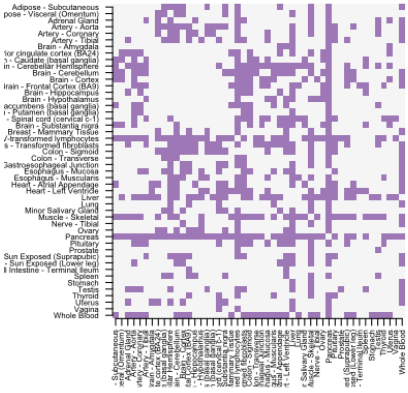

(b) GoM thin 0.01

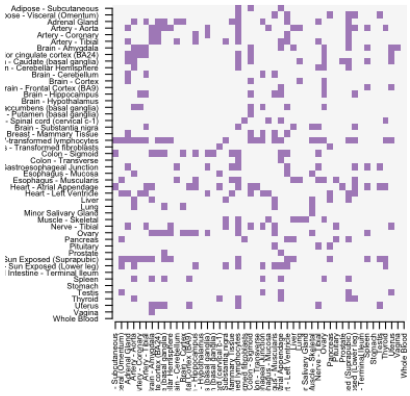

(c) hierarchy 0.0001

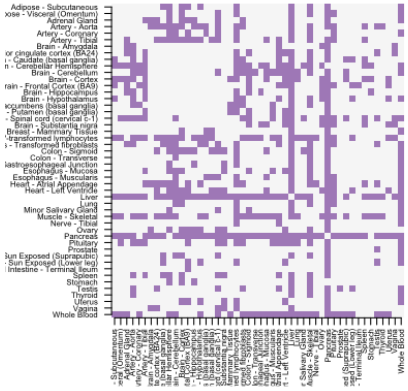

(d) GoM thin 0.0001

bioRxiv preprint doi: https://doi.org/10.1101/051631; this version posted May 4, 2016. The copyright holder for this preprint (which was not certified by peer review) is the author/funder, who has granted bioRxiv a license to display the preprint in perpetuity. It is made available under aCC-BY-NC-ND 4.0 International license.

7 Supplementary tables

S1 Table. Cluster Annotations GTEx V6 data (with top gene summaries).

Cluster	Top Driving Genes	Gene names	Gene Summary
1, Royal purple	*NEAT1*	nuclear paraspeckle assembly transcript 1	produces a long non-coding RNA (lncRNA) transcribed from the multiple endocrine neoplasia locus, regulates genes involved in cancer progression.
	CCNL2	cyclin L2	regulator of the pre-mRNA splicing process, as well as in inducing apoptosis by modulating the expression of apoptotic and antiapoptotic proteins.
	SRSF5	serine/arginine-rich splicing factor 5	encodes proteins of serine/arginine (SR)-rich family, involved in mRNA export from the nucleus and in translation.
2, Light purple	*SNAP25*	synaptosomal-associated protein, 25kDa	this gene product is a presynaptic plasma membrane protein involved in the regulation of neurotransmitter release.
	FBXL16	F-box and leucine-rich repeat protein 16	members of F-box protein family, which interact with SKP1 through the F box, and they interact with ubiquitination targets through other protein interaction domains.
	SLC17A7	neurochondrin	encodes proteins expressed in neuron-rich regions; associated with the membranes of synaptic vesicles and functions in glutamate transport.
3, Red	*FABP4*	fatty acid binding protein 4	encodes the fatty acid binding protein found in adipocytes, takes part in fatty acid uptake, transport, and metabolism.
	PLIN1	perilipin 1	protein encoded by this gene coats lipid storage droplets in adipocytes, thereby protecting them until they can be broken down by hormone-sensitive lipase.
	FASN	fatty acid synthase	catalyze the synthesis of palmitate from acetyl-CoA and malonyl-CoA, in the presence of NADPH, into long-chain saturated fatty acids.
4, Salmon	*ACTG2*	actin, gamma 2, smooth muscle, enteric	involved in various types of cell motility and in the maintenance of the cytoskeleton.
	MYH11	myosin, heavy chain 11, smooth muscle	protein encoded by this gene is a smooth muscle myosin belonging to the myosin heavy chain family, functions as a major contractile protein, converting chemical energy into mechanical energy through the hydrolysis of ATP.
	SYNM	synemin	protein has been found to form a linkage between desmin, which is a subunit of the IF network, and the extracellular matrix, and provides an important structural support in muscle.
5, Denim	*RGS5*	regulator of G-protein signaling 5	encodes a member of the regulators of G protein signaling (RGS) family, associated with retinal arterial macroaneurysm.
	MFGE8	milk fat globule-EGF factor 8 protein	encodes a preproprotein that is proteolytically processed to form multiple protein products, been implicated in wound healing, autoimmune disease, and cancer
	ITGA8	synemin	Proteins generated mediate numerous cellular processes including cell adhesion, cytoskeletal rearrangement, and activation of cell signaling pathways.
6, Light denim	*KRT10*	keratin 10	encodes a member of the type I (acidic) cytokeratin family, mutations associated with epidermolytic hyperkeratosis.
	KRT1	keratin 1, type II	specifically expressed in the spinous and granular layers of the epidermis with family member KRT10 and mutations in these genes have been associated with bullous congenital ichthyosiform erythroderma.
	KRT2	keratin 2, type II	expressed largely in the upper spinous layer of epidermal keratinocytes and mutations in this gene have been associated with bullous congenital ichthyosiform erythroderma.
7, Orange	*NEB*	nebulin	encodes nebulin, a giant protein component of the cytoskeletal matrix that coexists with the thick and thin filaments within the sarcomeres of skeletal muscle, associated with recessive nemaline myopathy.
	MYH1	myosin, heavy chain 1, skeletal muscle, adult	a major contractile protein which converts chemical energy into mechanical energy through the hydrolysis of ATP.
	MYH2	myosin, heavy chain 2, skeletal muscle, adult	encodes a member of the class II or conventional myosin heavy chains, and functions in skeletal muscle contraction.

bioRxiv preprint doi: https://doi.org/10.1101/051631; this version posted May 4, 2016. The copyright holder for this preprint (which was not certified by peer review) is the author/funder, who has granted bioRxiv a license to display the preprint in perpetuity. It is made available under aCC-BY-NC-ND 4.0 International license.

Cluster	Top Driving Genes	Gene namese	Gene Summary
8, Light orange	*FN1*	fibronectin 1	Fibronectin is involved in cell adhesion, embryogenesis, blood coagulation, host defense, and metastasis.
	COL1A1	collagen, type I, alpha 1	Mutations in this gene associated with osteogenesis imperfecta types I-IV, Ehlers-Danlos syndrome type and Classical type, Caffey Disease.
	COL1A2	collagen, type I, alpha 2	Mutations in this gene associated with osteogenesis imperfecta types I-IV, Ehlers-Danlos syndrome type and Classical type, Caffey Disease.
9, Green	*MBP*	myelin basic protein	major constituent of the myelin sheath of oligodendrocytes and Schwann cells in the nervous system
	GFAP	glial fibrillary acidic protein	encodes one of the major intermediate filament proteins of mature astrocytes, mutations casuses Alexander disease.
	CARNS1	carnosine synthase 1	catalyzes the formation of carnosine and homocarnosine, which are found mainly in skeletal muscle and the central nervous system, respectively.
10, Light green	*CYP17A1*	cytochrome P450 family 17 subfamily A member 1	encodes a member of the cytochrome P450 superfamily of enzymes, mutations in this gene are associated with isolated steroid-17 alpha-hydroxylase deficiency,20-lyase deficiency, pseudohermaphroditism, and adrenal hyperplasia.
	CYP11B1	cytochrome P450 family 11 subfamily B member 1	The protein encoded by this gene plays a key role in the acute regulation of steroid hormone synthesis by enhancing the conversion of cholesterol into pregnenolone, associated with congenital lipoid adrenal hyperplasia.
	GKN1	gastrokine 1	protein encoded by this gene is found to be down-regulated in human gastric cancer tissue as compared to normal gastric mucosa..
11, Turquoise	*MPZ*	myelin protein zero	specifically expressed in Schwann cells of the peripheral nervous system and encodes a type I transmembrane glycoprotein that is a major structural protein of the peripheral myelin sheath, mutations associated with autosomal dominant form of Charcot-Marie-Tooth disease type 1 and other polyneuropathies.
	APOD	apolipoprotein D	encodes a component of high density lipoprotein that has no marked similarity to other apolipoprotein sequences, closely associated with lipoprotein metabolism.
	PMP22	peripheral myelin protein 22	encodes an integral membrane protein that is a major component of myelin in the peripheral nervous system..
12, Yellow	*IGHM*	immunoglobulin heavy constant mu	IgM antibodies play an important role in primary defense mechanisms, Diseases associated with IGHM include agammaglobulinemia 1 and immunodeficiency 23.
	IGHG1	immunoglobulin heavy constant gamma 1 (G1m marker)	antigen binding functionality, diseases associated with IGHG1 include heavy chain deposition disease and chronic lymphocytic leukemia.
	IGHG2	immunoglobulin heavy constant gamma 2 (G2m marker)	antigen binding gene, diseases associated with IGHG2 include c2 deficiency.
13, Sky blue	*TG*	thyroglobulin	thyroglobulin produced predominantly in thyroid gland, synthesizes thyroxine and triiodothyronine, associated with Graves disease and Hashimotot thyroiditis.
	PRL	prolactin 2	encodes the anterior pituitary hormone prolactin. This secreted hormone is a growth regulator for many tissues, including cells of the immune system.
	PRM2	protamine 2	Protamines are the major DNA-binding proteins in the nucleus of sperm.
14, Light pink	*NPPA*	natriuretic peptide A	protein encoded by this gene belongs to the natriuretic peptide family, controls extracellular fluid volume and electrolyte homeostasis, mutations Mutations associated with atrial fibrillation familial type 6.
	MYH6	myosin, heavy chain 6, cardiac muscle, alpha	encodes the alpha heavy chain subunit of cardiac myosin, mutations cause familial hypertrophic cardiomyopathy and atrial septal defect 3
	TNNT2	protamine 2	protein encoded by this gene is the tropomyosin-binding subunit of the troponin complex, mutations in this gene have been associated with familial hypertrophic cardiomyopathy as well as with dilated cardiomyopathy.

bioRxiv preprint doi: https://doi.org/10.1101/051631; this version posted May 4, 2016. The copyright holder for this preprint (which was not certified by peer review) is the author/funder, who has granted bioRxiv a license to display the preprint in perpetuity. It is made available under aCC-BY-NC-ND 4.0 International license.

Cluster	Top Driving Genes	Gene namese	Gene Summary
15, Light gray	*KRT13*	keratin 13, type I	protein encoded by this gene is a member of the keratin gene family, associated with the autosomal dominant disorder White Sponge Nevus.
	KRT4	keratin 4, type II	protein encoded by this gene is a member of the keratin gene family, associated with White Sponge Nevus, characterized by oral, esophageal, and anal leukoplakia.
	CRNN	cornulin	may play a role in the mucosal/epithelial immune response and epidermal differentiation.
16, Gray	*SFTPB*	surfactant protein B	an amphipathic surfactant protein essential for lung function and homeostasis after birth, muttaions cause pulmonary alveolar proteinosis, fatal respiratory distress in the neonatal period.
	SFTPA2	surfactant protein A2	Mutations in this gene and a highly similar gene located nearby, which affect the highly conserved carbohydrate recognition domain, are associated with idiopathic pulmonary fibrosis.
	SFTPA1	surfactant protein A1	encodes a lung surfactant protein that is a member of C-type lectins called collectins, associated with idiopathic pulmonary fibrosis.
17, Brown	*CSF3R*	colony stimulating factor 3 receptor	protein encoded by this gene is the receptor for colony stimulating factor 3, a cytokine that controls the production, differentiation, and function of granulocytes, mutations a cause of Kostmann syndrome
	MMP25	matrix metallopeptidase 25	proteins are involved in the breakdown of extracellular matrix in normal physiological processes, such as embryonic development, reproduction, and tissue remodeling, as well as in disease processes, such as arthritis and metastasis.
	IL1R2	interleukin 1 receptor type 2	protein encoded by this gene is a cytokine receptor that belongs to the interleukin 1 receptor family.
18, Purple	*PRSS1*	protease, serine 1	secreted by pancreas, associated with pancreatitis
	CPA1	carboxypeptidase A1	secreted by pancreas, linked to pancreatitis and pancreatic cancer
	PNLIP	pancreatic lipase	encodes a carboxyl esterase that hydrolyzes insoluble, emulsified triglycerides, and is essential for the efficient digestion of dietary fats. This gene is expressed specifically in the pancreas.
19, Pink	*HBB*	hemoglobin, beta	mutant beta globin causes sickle cell anemia, absence of beta chain/ reduction in beta globin leads to thalassemia.
	HBA2	hemoglobin, alpha 2	deletion of alpha genes may lead to alpha thalassemia.
	HBA1	hemoglobin, alpha 1	deletion of alpha genes may lead to alpha thalassemia.
20, Dark gray	*ALB*	albumin	functions primarily as a carrier protein for steroids, fatty acids, and thyroid hormones and plays a role in stabilizing extracellular fluid volume.
	HP	haptoglobin	encodes a preproprotein, which subsequently produces haptoglobin, linked to diabetic nephropathy, Crohn's disease, inflammatory disease behavior and reduced incidence of Plasmodium falciparum malaria.
	FGB	fibrinogen beta chain	protein encoded by this gene is the beta component of fibrinogen, mutations may lead to several disorders, including afibrinogenemia, dysfibrinogenemia, hypodysfibrinogenemia etc.

bioRxiv preprint doi: https://doi.org/10.1101/051631; this version posted May 4, 2016. The copyright holder for this preprint (which was not certified by peer review) is the author/funder, who has granted bioRxiv a license to display the preprint in perpetuity. It is made available under aCC-BY-NC-ND 4.0 International license.

S2 Table. **Cluster Annotations GTEx V6 Brain data (with top gene summaries).**

Cluster	Top Driving Genes	Gene names	Gene Summary
1, Royal blue	*CLU*	clusterin	protein encoded by this gene is a secreted chaperone that can under some stress conditions also be found in the cell cytosol, also involved in cell death, tumor progression, and neurodegenerative disorders.
	OXT	oxytocin/neurophysin I prepropeptide	encodes a precursor protein that is processed to produce oxytocin and neurophysin I, involved in contraction of smooth muscle during parturition and lactation, cognition, tolerance, adaptation and complex sexual and maternal behaviour.
	GLUL	glutamate-ammonia ligase	catalyzes the synthesis of glutamine from glutamate and ammonia in an ATP-dependent reaction, associated with congenital glutamine deficiency, and overexpression of this gene was observed in some primary liver cancer samples.
2, Turquoise	*ENC1*	ectodermal-neural cortex 1	plays a role in the oxidative stress response as a regulator of the transcription factor Nrf2, may play role in malignant transformation.
	NCALD	neurocalcin delta	encodes a member of the neuronal calcium sensor (NCS), a regulator of G protein-coupled receptor signal transduction.
	YWHAH	tyrosine 3-monooxygenase/tryptophan 5-monooxygenase activation protein eta	mediate signal transduction by binding to phosphoserine-containing proteins, associated with early-onset schizophrenia and psychotic bipolar disorder.
3, Lime green	*PKD1*	polycystin 1, transient receptor potential channel interacting	functions as a regulator of calcium permeable cation channels and intracellular calcium homoeostasis. It is also involved in cell-cell/matrix interactions and may modulate G-protein-coupled signal-transduction pathways.
	CBLN3	cerebellin 3 precursor	contain a cerebellin motif and C-terminal C1q signature domain that mediates trimeric assembly of atypical collagen complexes
	CHGB	chromogranin B	encodes a tyrosine-sulfated secretory protein abundant in peptidergic endocrine cells and neurons. This protein may serve as a precursor for regulatory peptides.
4, Red	*PPP1R1B*	protein phosphatase 1 regulatory inhibitor sub- unit 1B	encodes a bifunctional signal transduction molecule, may serve as a therapeutic target for neurologic and psychiatric disorders.
	RGS14	regulator of G-protein signaling 14	attenuates the signaling activity of G-proteins, increases the rate of conversion of the GTP to GDP.
	NCDN	neurochondrin	encodes a leucine-rich cytoplasmic protein, essential for spatial learning processes.
5, Yellow orange	*MBP*	myelin basic protein	protein encoded is a major constituent of the myelin sheath of oligodendrocytes and Schwann cells in the nervous system.
	GFAP	glial fibrillary acidic protein	encodes major intermediate filament proteins of mature astrocytes, a marker to distinguish astrocytes during development, mutations in this gene cause Alexander disease, a rare disorder of astrocytes in central nervous system.
	TF	transferrin	transport iron from the intestine, reticuloendothelial system, and liver parenchymal cells to all proliferating cells in the body, involved in the removal of certain organic matter and allergens from serum.
6, Yellow	*IQGAP1*	IQ motif containing GTPase activating protein 1	interacts with components of the cytoskeleton, with cell adhesion molecules, and with several signaling molecules to regulate cell morphology and motility.
	A2M	alpha-2-macroglobulin	inhibits many proteases, including trypsin, thrombin and collagenase. A2M is implicated in Alzheimer disease (AD) due to its ability to mediate the clearance and degradation of A-beta, the major component of beta-amyloid deposits.
	C3	complement component 3	plays a central role in the activation of complement system, associated with atypical hemolytic uremic syndrome and age-related macular degeneration in human patients.

bioRxiv preprint doi: https://doi.org/10.1101/051631; this version posted May 4, 2016. The copyright holder for this preprint (which was not certified by peer review) is the author/funder, who has granted bioRxiv a license to display the preprint in perpetuity. It is made available under aCC-BY-NC-ND 4.0 International license.

S3 Table. **Deng et al (2014) Cluster 1 (blue) top GO annotations.**

	go.id	name	significant
1	GO:0007276	gamete generation	BCL2L10; GDF9; NOBOX; PABPC1L; RGS2; CREB3L4; RNF114; BMP15; PTTG1; TDRD12; WEE2; SPIN1; DAZL
2	GO:0007292	female gamete generation	GDF9; BCL2L10; PABPC1L; BMP15; WEE2; DAZL; NOBOX
3	GO:0048609	multicellular organismal reproductive process	GDF9; NOBOX; PABPC1L; BCL2L10; BMP15; CREB3L4; TGFB2; RNF114; RGS2; PTTG1; TDRD12; WEE2; SPIN1; DAZL
4	GO:0032504	multicellular organism reproduction	GDF9; NOBOX; PABPC1L; BCL2L10; BMP15; CREB3L4; TGFB2; RNF114; RGS2; PTTG1; TDRD12; WEE2; SPIN1; DAZL
5	GO:0019953	sexual reproduction	BCL2L10; GDF9; NOBOX; PABPC1L; RGS2; CREB3L4; RNF114; BMP15; PTTG1; TDRD12; WEE2; SPIN1; DAZL
6	GO:0044702	single organism reproductive process	GDF9; NOBOX; PABPC1L; BCL2L10; BMP15; CREB3L4; TGFB2; CASP8; RNF114; RGS2; PTTG1; TDRD12; WEE2; SPIN1; DAZL
7	GO:0048477	oogenesis	WEE2; GDF9; NOBOX; PABPC1L; DAZL
8	GO:0044703	multi-organism reproductive process	BCL2L10; GDF9; NOBOX; PABPC1L; RGS2; CREB3L4; RNF114; BMP15; PTTG1; TDRD12; WEE2; SPIN1; DAZL
9	GO:0048599	oocyte development	WEE2; GDF9; PABPC1L; DAZL
10	GO:0009994	oocyte differentiation	WEE2; GDF9; PABPC1L; DAZL
11	GO:0051321	meiotic cell cycle	H1FOO; WEE2; TDRD12; SPIN1; PTTG1; DAZL
12	GO:0001556	oocyte maturation	WEE2; PABPC1L; DAZL
13	GO:0006306	DNA methylation	TDRD12; H1FOO; TET3; ZFP57
14	GO:0051302	regulation of cell division	TGFB2; PTTG1; TXNIP; WEE2; CHEK1; DAZL
15	GO:0060255	regulation of macromolecule metabolic process	TGFB2; NOBOX; BPGM; UBE2D3; NFYA; CASP8; BMP15; TXNIP; TDRD12; GDF9; BCL2L10

S3 Table continued. **Deng et al (2014) Cluster 2 (magenta) top GO annotations.**

	go.id	name	significant
1	GO:0016604	nuclear body	YTHDC1; RBM8A; CDK12; PSME4; PPP1R8; HIPK1; TOPORS
2	GO:0005814	centriole	SFI1; PLK2; ROCK1; TOPORS
3	GO:0044450	microtubule organizing center part	SFI1; PLK2; ROCK1; TOPORS

bioRxiv preprint doi: https://doi.org/10.1101/051631; this version posted May 4, 2016. The copyright holder for this preprint (which was not certified by peer review) is the author/funder, who has granted bioRxiv a license to display the preprint in perpetuity. It is made available under aCC-BY-NC-ND 4.0 International license.

S3 Table continued. **Deng et al (2014) Cluster 3 (yellow) top GO annotations.**

	go.id	name	significant
1	GO:0044428	nuclear part	MAD2L2; SMARCC1; PPRC1; SLU7; NFYB; TOR1B; MIOS; NR1H3; POLR3K
2	GO:0031981	nuclear lumen	MAD2L2; SMARCC1; PPRC1; SLU7; NFYB; POLR1E; MIOS; POLR3K; XPO1
3	GO:0070013	intracellular organelle lumen	MAD2L2; SMARCC1; PPRC1; SLU7; NFYB; POLR1E; MIOS; POLR3K; XPO1; DNTTIP2; ZBTB10; ZBTB17
4	GO:0043233	organelle lumen	MAD2L2; SMARCC1; PPRC1; SLU7; NFYB; POLR1E; MIOS; POLR3K; XPO1
5	GO:0005730	nucleolus	XPO1; DNTTIP2; ESF1; WDR43; ZDHHC7; HEATR1; POLR1E; DDX24; POLR3K
6	GO:0005634	nucleus	MAD2L2; SMARCC1; PPRC1; SLU7; NFYB; TOR1B; MIOS; NR1H3; EIF5B; POLR3K
7	GO:0044446	intracellular organelle part	MAD2L2; PTDSS2; SMARCC1; KLHL21; TOR1B; PPRC1; SLU7; NFYB; SLC25A36; ECE2
8	GO:0005654	nucleoplasm	MAD2L2; SMARCC1; PPRC1; SLU7; NFYB; POLR1E; MIOS; POLR3K; XPO1; ZBTB10; ZBTB17
9	GO:0003723	RNA binding	PPRC1; EIF5B; XPO1; DNTTIP2; WDR43; DDX10; EIF3C; BCLAF1; EBNA1BP2; RARS
10	GO:0003676	nucleic acid binding	SMARCC1; PPRC1; SLU7; NFYB; POLR1E; EIF5B; POLR3K; XPO1; DNTTIP2
11	GO:0043231	intracellular membrane-bounded organelle	MAD2L2; PTDSS2; SMARCC1; TOR1B; PPRC1; SLU7; NFYB; ESF1; ECE2; LMAN1L
12	GO:0043229	intracellular organelle	MAD2L2; PTDSS2; SMARCC1; KLHL21; TOR1B; PPRC1; ARRDC1; SLU7; NFYB; ESF1; ECE2
13	GO:0005874	microtubule	WDR43; KLHL21; HAUS6; CENPE; TEKT2; RACGAP1; WDR81; BCL2L11; KIF20B
14	GO:0044822	poly(A) RNA binding	WDR43; DNTTIP2; ESF1; NXF1; DDX10; HEATR1; EIF3C
15	GO:0044424	intracellular part	MAD2L2; PTDSS2; SMARCC1; KLHL21; TOR1B; PPRC1; SNAPC4; POLR3K; ARRDC1; SLU7; NFYB; ESF1; WDR43; ECE2; LMAN1L

bioRxiv preprint doi: https://doi.org/10.1101/051631; this version posted May 4, 2016. The copyright holder for this preprint (which was not certified by peer review) is the author/funder, who has granted bioRxiv a license to display the preprint in perpetuity. It is made available under aCC-BY-NC-ND 4.0 International license.

S3 Table continued. **Deng et al (2014) Cluster 4 (green) top GO annotations.**

	go.id	name	significant
1	GO:0005829	cytosol	PARG; UAP1; PSMB10; TCEB1; RPLP0; EIF5; CNBP; RPS3; PSAT1; AACS; PMM1; EXOSC7; EIF3I; SET; BHMT; BHMT2
2	GO:0044444	cytoplasmic part	PARG; UAP1; PSMB10; TCEB1; HSPA8; SERINC1; EIF5; CNBP; RPS3; PSAT1; GPD2; AACS; GPR137B; STIP1; PMM1; EXOSC7; VPREB3; PEX16
3	GO:0055131	C3HC4-type RING finger domain binding	HSPA8; PINK1; DNAJA1
4	GO:1901575	organic substance catabolic process	PSMB10; TCEB1; RPLP0; RPS3; GPD2; PINK1; EXOSC7; ALLC; BHMT; HSP90AB1; RPL13A; ATG7; CUL5; UBXN1; ZMPSTE24
5	GO:0000151	ubiquitin ligase complex	DNAJA1; RNF7; UBE2C; HSPA8; FBXO15; SUGT1; DCAF4; CUL5; FBXL20
6	GO:0072655	protein localization to mitochondrion	TIMM17A; BNIP3L; ARIH2; PEMT; SFN; PINK1; HSP90AA1; TIMM23
7	GO:1901564	organonitrogen compound metabolic process	PSMB10; RPLP0; SERINC1; EIF5; BHMT2; PINK1; EIF3I; ALLC; BHMT; MRPL22; RPL13A; ATG7; NUDT9; VNN1; CTSA; HK1
8	GO:0005737	cytoplasm	PARG; UAP1; PSMB10; TCEB1; HSPA8; SERINC1; EIF5; CNBP; RPS3; PSAT1; GPD2; AACS; GPR137B; STIP1; PMM1; EXOSC7
9	GO:0044265	cellular macromolecule catabolic process	EXOSC7; SUMO2; BNIP3L; ARIH2; PSMB10; TCEB1; RPLP0; UBXN1; HSP90AB1; RPL13A; RPS3; RNF7; PINK1
10	GO:0023026	MHC class II protein complex binding	HSP90AB1; HSP90AA1; HSPA8
11	GO:0051082	unfolded protein binding	DNAJA1; PTGES3; HSPA8; HSP90AB1; HSP90AA1; NPM1
12	GO:0009056	catabolic process	PSMB10; TCEB1; RPLP0; RPS3; GPD2; PINK1; EXOSC7; ALLC; WDR45; HSP90AB1; RPL13A
13	GO:0009057	macromolecule catabolic process	EXOSC7; SUMO2; BNIP3L; ARIH2; PSMB10; TCEB1; RPLP0; AZIN1; UBXN1; HSP90AB1; RPL13A
14	GO:0044248	cellular catabolic process	PSMB10; TCEB1; SUMO2; RPS3; GPD2; PINK1; EXOSC7; ALLC; WDR45; HSP90AB1
15	GO:0006626	protein targeting to mitochondrion	TIMM17A; BNIP3L; ARIH2; PEMT; PINK1; HSP90AA1; TIMM23

bioRxiv preprint doi: https://doi.org/10.1101/051631; this version posted May 4, 2016. The copyright holder for this preprint (which was not certified by peer review) is the author/funder, who has granted bioRxiv a license to display the preprint in perpetuity. It is made available under aCC-BY-NC-ND 4.0 International license.

S3 Table continued. **Deng et al (2014) Cluster 5 (purple) top GO annotations.**

	go.id	name	significant
1	GO:0044710	single-organism metabolic process	PCK2; SAT1; EPHX2; NFATC4; CKB; PRDX6; MSH2; EPHA4; PROS1; PDGFRA; PRDX1; UBE2L6; POGLUT1; FABP5; AKAP12; TDGF1; FBP2; SOX2
2	GO:0006950	response to stress	EPHX2; NFATC4; PRDX6; MSH2; EPHA4; PROS1; PDGFRA; PRDX1; UBE2L6; FABP5; TDGF1; SOX2
3	GO:0065010	extracellular membrane-bounded organelle	PCK2; EPHX2; MFGE8; CKB; PRDX6; PROS1; PRDX1; POGLUT1; FABP5; FBP2; TRAP1; PLOD2; DHRS4
4	GO:0070062	extracellular exosome	PCK2; EPHX2; MFGE8; CKB; PRDX6; PROS1; PRDX1; POGLUT1; FABP5; FBP2; TRAP1; PLOD2; DHRS4; MARCKS; DPP4; PRKCI; RAC2; IDH1
5	GO:0043230	extracellular organelle	PCK2; EPHX2; MFGE8; CKB; PRDX6; PROS1; PRDX1; POGLUT1; FABP5; FBP2; TRAP1; PLOD2; DHRS4; MARCKS; DPP4
6	GO:1903561	extracellular vesicle	PCK2; EPHX2; MFGE8; CKB; PRDX6; PROS1; PRDX1; POGLUT1; FABP5; FBP2; TRAP1; PLOD2; DHRS4; MARCKS; DPP4; PRKCI
7	GO:0042221	response to chemical	EPHX2; NFATC4; MFGE8; PRDX6; EPHA4; PROS1; PDGFRA; PRDX1; UBE2L6; TDGF1; SOX2
8	GO:0031988	membrane-bounded vesicle	PCK2; EPHX2; MFGE8; CKB; PRDX6; PROS1; PRDX1; POGLUT1; FABP5; FBP2; TRAP1; PLOD2; DHRS4; SPARC
9	GO:0031982	vesicle	PCK2; EPHX2; MFGE8; CKB; PRDX6; PROS1; PRDX1; POGLUT1; FABP5; FBP2; TRAP1; PLOD2; DHRS4; SPARC
10	GO:0001525	angiogenesis	SAT1; PDGFRA; BMP4; NFATC4; MFGE8; FN1; MEIS1; SPARC; COL4A2; COL4A1; FGF10; TDGF1
11	GO:0048514	blood vessel morphogenesis	SAT1; PDGFRA; BMP4; NFATC4; MFGE8; FN1; ZFP36L1; MEIS1; SPARC; COL4A2; COL4A1; FGF10; TDGF1
12	GO:0001944	vasculature development	SAT1; PDGFRA; BMP4; NFATC4; MFGE8; FN1; ZFP36L1; MEIS1; PDPN; SPARC; COL4A2; COL4A1; FGF10; TDGF1
13	GO:0006979	response to oxidative stress	TAT; PDGFRA; BMP4; ETV5; TRAP1; PRDX6; IDH1; PARP1; AQP8; PRDX1; CRYGD
14	GO:0009725	response to hormone	PRKCI; GJA1; PDGFRA; BMP4; MFGE8; TAT; PLOD2; SPP1; IDH1
15	GO:0030198	extracellular matrix organization	PDGFRA; BMP4; JAM2; FN1; PLOD2; SPARC; SPP1; COL4A2; COL4A1; SERPINH1; DPP4

bioRxiv preprint doi: https://doi.org/10.1101/051631; this version posted May 4, 2016. The copyright holder for this preprint (which was not certified by peer review) is the author/funder, who has granted bioRxiv a license to display the preprint in perpetuity. It is made available under aCC-BY-NC-ND 4.0 International license.

S3 Table continued. **Deng et al (2014) Cluster 6 (orange) top GO annotations.**

	go.id	name	genes
1	GO:0065010	extracellular membrane-bounded organelle	MYH10; SLC2A3; GM2A; TSPAN8; ACTG1; SDC4; TINAGL1; CRYAB; MSN; FABP3; PDZK1IP1; PRSS8; S100A11; DAB2; KRT8; LCP1; UGP2
2	GO:0070062	extracellular exosome	MYH10; SLC2A3; GM2A; TSPAN8; ACTG1; SDC4; TINAGL1; CRYAB; MSN; FABP3; PDZK1IP1; PRSS8; S100A11; DAB2; KRT8; LCP1; UGP2
3	GO:0043230	extracellular organelle	MYH10; SLC2A3; GM2A; TSPAN8; ACTG1; SDC4; TINAGL1; CRYAB; MSN; FABP3; PDZK1IP1; PRSS8; S100A11
4	GO:1903561	extracellular vesicle	MYH10; SLC2A3; GM2A; TSPAN8; ACTG1; SDC4; TINAGL1; CRYAB; MSN; FABP3; PDZK1IP1; PRSS8; S100A11; DAB2; KRT8
5	GO:0031988	membrane-bounded vesicle	MYH10; SLC2A3; GM2A; TSPAN8; ACTG1; TMSB4X; SDC4; TINAGL1; CRYAB; MSN; FABP3; PDZK1IP1; PRSS8; S100A11; DAB2
6	GO:0031982	vesicle	MYH10; SLC2A3; GM2A; TSPAN8; ACTG1; TMSB4X; SDC4; TINAGL1; CRYAB; MSN; FABP3; PDZK1IP1; PRSS8; S100A11; DAB2; KRT8
7	GO:0008092	cytoskeletal protein binding	MYH10; TPM4; TMSB4X; CRYAB; MSN; TMSB10; FABP3; NDRG1; CALM1; FMNL2; MYH9; CAP1; TPM1; CDH1
8	GO:0015629	actin cytoskeleton	MYH10; CLIC4; MYH9; MYL12B; WDR1; CNN2; ARPC2; AHNAK; ACTN4; CRYAB; CAP1; TPM1; DSTN; ARPC5; TPM4
9	GO:0003779	actin binding	MYH10; TPM4; WDR1; CNN2; FMNL2; ARPC2; MYH9; CAP1; TPM1
10	GO:0048468	cell development	MYH10; CAPG; ACTG1; WDR1; CNN2; FMNL2; MYH9; ACTN4; SDC4; CAP1; TPM1; DSTN
11	GO:0030036	actin cytoskeleton organization	MYH10; CAPG; ACTG1; WDR1; CNN2; FMNL2; MYH9; ACTN4; SDC4; CAP1; TPM1
12	GO:0032432	actin filament bundle	MYH10; TPM4; MYL12B; CNN2; MYH9; CRYAB; TPM1; ACTN4; LCP1
13	GO:0005912	adherens junction	TJP2; MYH9; ACTG1; CNN2; ARPC2; AHNAK; ACTN4; SDC4
14	GO:0070161	anchoring junction	TJP2; MYH9; ACTG1; CNN2; ARPC2; AHNAK; ACTN4; SDC4
15	GO:0005925	focal adhesion	MYH9; ACTG1; CNN2; ARPC2; AHNAK; ACTN4; SDC4; CAP1; ARPC5